scientific reports

OPEN

Highly efficient emerging Ag$_2$BaTiSe$_4$ solar cells using a new class of alkaline earth metal-based chalcogenide buffers alternative to CdS

Kaviya Tracy Arockiya Dass[1], M. Khalid Hossain[2] & Latha Marasamy[1]✉

Cu$_2$ZnSn(S,Se)$_4$ is a non-toxic, earth-abundant photovoltaic absorber. However, its efficiency is limited by a large open circuit voltage (V$_{OC}$) deficit occurring due to its antisite defects and improper band alignment with toxic CdS buffer. Therefore, finding an absorber and non-toxic buffers that reduce V$_{OC}$ deficit is crucial. Herein, for the first time, Ag$_2$BaTiSe$_4$ is proposed as an alternative absorber using SCAPS-1D wherein a new class of alkaline earth metal chalcogenide such as MgS, CaS, SrS, and BaS is applied as buffers, and their characteristics are compared with CdS to identify their potential and suitability. The buffer and absorber properties are elucidated by tuning their thickness, carrier concentration, and defect density. Interestingly, optimization of the buffer's carrier concentration suppressed the barrier height and accumulation of charge carriers at the absorber/buffer interface, leading to efficiencies of 18.81%, 17.17%, 20.6%, 20.85%, 20.08% in MgS, CaS, SrS, BaS, and CdS-based solar cells respectively. Upon optimizing Ag$_2$BaTiSe$_4$, MoSe$_2$, and interface defects maximum efficiency of > 28% is achieved with less V$_{OC}$ loss (~ 0.3 V) in all solar cells at absorber's thickness, carrier concentration, and defect density of 1 μm, 10^{18} cm^{-3}, 10^{15} cm^{-3} respectively, underscoring the promising nature of Ag$_2$BaTiSe$_4$ absorber and new alkaline earth metal chalcogenide buffers in photovoltaics.

The world's population is growing at a rapid pace, and with technological advancements, there is a higher demand for energy in all sectors. Fossil fuels have been the primary source of energy, but their excessive usage is leading to environmental problems due to toxic gas emissions, and they are also becoming scarce[1,2]. This has caused a need for renewable sources of energy to cater to the increasing demand. Scientists have been researching the generation of solar energy through photovoltaic devices to produce electricity[3]. The most widely used solar cells are made from crystalline silicon, which has a high conversion efficiency and is thermally stable, besides being abundant in the earth's crust. However, their manufacturing cost is high because of the energy required for production[4]. Other materials used for solar cells such as CdTe and CIGSe have a lower payback period, are less expensive to produce, and have a higher efficiency, but their commercialization is limited due to their toxicity (Cd) or scarcity (In and Ga)[5,6]. CZTSSe of group I$_2$-II-IV-VI$_4$ is a promising alternative material for solar cells since it is non-toxic, has a high absorption coefficient, and its elements are available in abundance in the earth's crust[7]. However, CZTSSe solar cells have a lower efficiency of 14.9%, less than their theoretical limit of 31%, resulting from a high V$_{OC}$ deficit[8-10]. This is caused by antisite defects (Cu$_{Zn}$ and Zn$_{Cu}$), arising from the similar ionic size of Cu and Zn[11,12]. Through various experiments, researchers have attempted to suppress the antisite defects and enhance the efficiency of CZTSSe solar cells by altering its elements (Cu/Zn). For instance, Cu$_2$CdSnS$_4$ material demonstrated the highest PCE of over 10% where the toxicity of Cd is the major problem[13]. Other materials such as Cu$_2$FeSnS$_4$, Cu$_2$BaSn(S,Se)$_4$, Cu$_2$SrSnS$_4$, Cu$_2$CoSnS$_4$, Cu$_2$NiSnS$_4$, Cu$_2$MnSnS$_4$, Ag$_2$ZnSnS$_4$, and n-Ag$_2$ZnSnSe$_4$ were also studied[14-21]. But, the overall efficiency of these materials still falls short of CZTSSe solar cells.

Currently, scientists are exploring ways to enhance the efficiency of I$_2$-II-IV-VI$_4$ materials that are used in solar cells. Interestingly, they have discovered that a large density of Sn$_{Cu}$ and Sn$_{Zn}$ antisite defects are also present in

[1]Facultad de Química, Materiales-Energía, Universidad Autónoma de Querétaro, 76010 Santiago de Querétaro, QRO, México. [2]Institute of Electronics, Atomic Energy Research Establishment, Bangladesh Atomic Energy Commission, Dhaka 1349, Bangladesh. ✉email: latha.marasamy@uaq.mx

1

CZTSSe solar cells, which can have an adverse impact on their performance by increasing the recombination of charge carriers[22]. These defects are believed to be responsible for the V_{OC} deficit in these solar cells, indicating the need to modify group IV (Sn) elements in the cells along with group I and II (Cu/Zn) to enhance their efficiency. To address this issue, researchers have suggested $Ag_2BaTiSe_4$ as an alternative material[23]. This non-toxic and earth-abundant material possesses a suitable bandgap of 1.18 eV and remarkable optoelectronic properties. It exhibits a strong optical response in the visible and NIR regions, and the probability of the formation of group I, II, and IV elements-based antisite defects is comparatively low[23]. However, despite its ideal absorber properties, its applicability in photovoltaics has not been explored theoretically or experimentally. Therefore, further research is necessary to investigate its material characteristics and photovoltaic performance.

Furthermore, improper band alignment between absorber and buffer drastically affects the V_{OC} of I_2-II-IV-VI_4 solar cells[9]. CdS is a typical buffer that is used in many solar cells, but it contains toxic Cd, which makes it difficult to use in an industrial setting[24]. Researchers have tried using alternatives such as ZnMgO, ZnS, ZnO, Zn(S,O), and In_2S_3 where the native point defects, large series resistance, high interface recombination, difficulty in controlling the S-to-O ratio along with secondary phase formation, and the presence of rare earth element (In) are found to be their critical problems respectively[25–29]. There are non-toxic and earth-abundant options such as MgS, CaS, SrS, and BaS, which are alkaline earth metal-based chalcogenide semiconductors[30]. These materials have low reflectance, low absorbance, and high transmittance in the visible region, making them ideal buffers for thin-film solar cells. Moreover, they can be easily synthesized[31–35]. Although they have promising properties, it is not yet clear whether they are suitable for use as buffers in thin-film solar cells. This presents an excellent opportunity for the photovoltaic community to explore the properties of these materials as potential buffers in solar cells.

Scientists have used theoretical simulations to improve the design of solar cells by studying how different materials affect their performance[36]. The software used for this purpose is called Solar Cell Capacitance Simulator in One Dimension (SCAPS-1D), which can model solar cells and provide crucial information about how each layer of the cell influences its performance. This information includes details about the materials' properties, band alignment, interfacial defects, resistance, and the solar cell's stability[37]. SCAPS-1D has been used to simulate various types of solar cells, and its results have been consistent with experimental outcomes[37–39].

In our study, we used SCAPS-1D to explore the properties and functions of solar cells made with a new absorber called $Ag_2BaTiSe_4$ and new alkaline earth metal chalcogenide buffers such as MgS, CaS, SrS, and BaS. We also designed solar cells with the conventional CdS buffer to compare the performance of different buffers. We analyzed the impact of various factors on the solar cells, such as the thickness, carrier concentration, defect density of buffers, and $Ag_2BaTiSe_4$ absorber layer. We also investigated the role of $Ag_2BaTiSe_4$'s electron affinity and the influence of interfacial defects, parasitic resistance and working temperature on the solar cells' performance. Our research provides valuable insights into the potential of alkaline earth metal chalcogenides as alternative buffers and the properties of $Ag_2BaTiSe_4$ for the development of non-toxic, low-cost, and efficient thin-film solar cells.

Device structure and method

SCAPS-1D (version 3.3.10) is a solar cell simulation software used to extensively study the properties of each layer in the solar cell[40]. It was developed by Marc Burgelman in the Department of Electronics & Information Systems at the University of Gent, Belgium[41]. It is widely utilized to simulate various solar cells, including CdTe, CIGSe, CZTS, perovskites, etc.[42–44]. It assists the photovoltaic community by providing current density–voltage (J–V), capacitance–voltage (C–V), capacitance–frequency (C–F), quantum efficiency (QE), energy band diagram, carrier density, electric field, and recombination profiles of the modeled solar cells. In addition, other output parameters such as V_{OC}, short circuit current density (J_{SC}), fill factor (FF), and PCE corresponding to each layer's parameters can be analyzed. It performs these operations by solving three fundamental equations: Poisson, continuity, and transport equations of charge carriers integrated in SCAPS-1D software[45]. Poisson (Eq. 1), continuity (Eq. 2 and Eq. 3), and charge transport (Eq. 4 and Eq. 5) equations of charge carriers are provided below:

$$\frac{\partial^2 \varphi(x)}{\partial x^2} = \frac{q}{\varepsilon}\left(n(x) - p(x) - N_D^+(x) + N_A^-(x) - p_t(x) + N_t(x)\right) \tag{1}$$

$$\frac{\partial n}{\partial t} = \frac{1}{q}\frac{\partial J_n}{\partial x} + (G_n - R_n) \tag{2}$$

$$\frac{\partial p}{\partial t} = -\frac{1}{q}\frac{\partial J_p}{\partial x} + \left(G_p - R_p\right) \tag{3}$$

$$J_n = qD_n\frac{\partial n}{\partial x} - q\mu_n n\frac{\partial \varphi}{\partial x} \tag{4}$$

$$J_p = qD_p\frac{\partial p}{\partial x} - q\mu_p p\frac{\partial \varphi}{\partial x} \tag{5}$$

where q, ε, p, n, N_D^+, N_A^-, G_n, G_p, R_n, R_p, φ, D_n, D_p, J_p, J_n, μ_n, and μ_p are elemental charge, dielectric constant, hole concentration, electron concentration, donor-type doping concentration, acceptor-type doping concentration, generation rate of electrons, generation rate of holes, recombination rate of electrons, recombination rate of holes,

electric potential, coefficient of electron diffusion, coefficient of hole diffusion, hole current density, electron current density, electron mobility, and hole mobility respectively.

In this work, we have investigated the performance of novel $Ag_2BaTiSe_4$ solar cells with five buffers: MgS, CaS, SrS, BaS, and CdS, using SCAPS-1D. It is simulated in substrate device configuration of front contact/Al:ZnO(AZO)/i-ZnO(IZO)/buffer/$Ag_2BaTiSe_4$/$MoSe_2$/Mo/glass as shown in Fig. 1a. The initial parameters of each layer used for the simulation of the solar cell are listed in Table 1. These parameters are taken from the literature[45–50]. In Table 1, E_g, χ, ε_r, N_C, N_V, μ_n, μ_p, N_D, N_A, N_t, SA, and SD represent bandgap, affinity, dielectric permittivity, effective density of states in the conduction band, effective density of states in the valence band, electron mobility, hole mobility, donor concentration, acceptor concentration, defect density, single acceptor, and single donor respectively. The thermal velocity of electrons and holes are fixed at 10^7 cm s^{-1} for all the layers, and flat band condition is applied to the front contact. The simulations are carried out at 300 K under AM 1.5G spectral irradiance, wherein shunt and series resistance are not considered. In addition, neutral defects are introduced at the $Ag_2BaTiSe_4$/$MoSe_2$ and buffer/$Ag_2BaTiSe_4$ interfaces according to the parameters listed in Table 2 to simulate realistic conditions of solar cells.

Throughout the simulation, the parameters of AZO and IZO were fixed according to Table 1. The thickness of AZO in thin-film solar cells usually ranges from 0.1 to 0.5 μm[51–56]. However, experimental results have shown that a thickness of 0.2 μm is optimal in terms of low resistivity, high mobility, and carrier concentration[57]. Therefore, we have chosen a thickness of 0.2 μm for the AZO layer. Similarly, for IZO, the optimal thickness for high solar cell performance is between 0.04 and 0.1 μm, as reported by experiments[51,53–55,58]. If the thickness is less than 0.04 μm, it increases the leakage current, while for a thickness greater than 0.1 μm, the series resistance increases and the built-in field reduces, leading to degraded performance[59–61]. Based on material usage and experimental range, we have selected a thickness of 0.05 μm for IZO. Likewise, the other material parameters of AZO and IZO were adapted from the experiments[57,61]. The important parameters of other layers such as buffers, $Ag_2BaTiSe_4$ and $MoSe_2$ were tuned to discover their optimum range and understand their influence on the solar cell performance.

To begin with, initial solar cells are designed with the parameters listed in Table 1. After that, the performance of the solar cells is studied as a function of buffer thickness (0.05 to 0.2 μm), carrier concentration (10^{12}
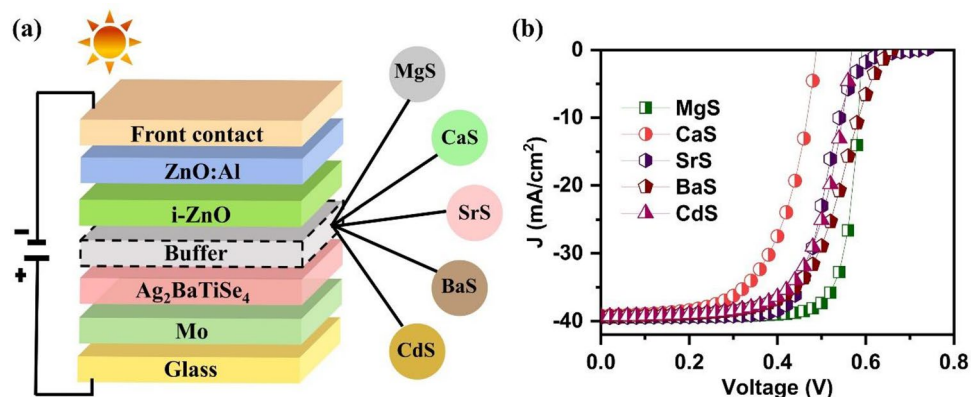

Figure 1. (**a**) Schematic structure of novel $Ag_2BaTiSe_4$ solar cells with diverse buffers. (**b**) Initial J–V of novel $Ag_2BaTiSe_4$ solar cells.

Parameters	Al:ZnO	i-ZnO	Ag₂BaTiSe₄	MoSe₂	Buffers				
					MgS	CaS	SrS	BaS	CdS
Thickness (μm)	0.200	0.050	1.0	0.050	0.080	0.080	0.080	0.080	0.080
E_g (eV)	3.40	3.40	1.18	1.4	2.7	2.14	2.5	3.0	2.42
χ (eV)	4.60	4.60	4.1	4.12	4.3	4.6	4.0	4.15	4.5
ε_r	9.00	9.00	6	8.76	10	9	10	15	9
N_C (cm^{-3})	2.0×10^{18}	2.0×10^{18}	1.0×10^{19}	2.8×10^{19}	1.9×10^{19}	2.9×10^{19}	1.2×10^{19}	1.2×10^{18}	1.8×10^{19}
N_V (cm^{-3})	1.8×10^{19}	1.8×10^{19}	1.0×10^{19}	2.65×10^{19}	1.0×10^{18}	1.0×10^{18}	1.4×10^{18}	1.4×10^{19}	2.4×10^{18}
μ_n (cm^2 Vs^{-1})	150	150	100	100	75	150	100	100	160
μ_h (cm^2 Vs^{-1})	25	25	250	250	50	50	25	25	50
N_A (cm^{-3})	0	0	1.0×10^{15}	1.0×10^{17}	0	0	0	0	0
N_D (cm^{-3})	1.0×10^{20}	1.0×10^{17}	0	0	1.0×10^{17}	1.0×10^{17}	1.0×10^{17}	1.0×10^{16}	1.0×10^{17}
N_t (cm^{-3})	1.0×10^{15}	1.0×10^{15}	1.0×10^{15}	1.0×10^{15}	1.0×10^{15}	1.0×10^{15}	1.0×10^{15}	1.0×10^{15}	1.0×10^{15}
Defect type	SA	SA	SD	SD	SA	SA	SA	SA	SA

Table 1. Input parameters of different layers of novel $Ag_2BaTiSe_4$ solar cells used in the simulation[45–50].

Parameters	Ag₂BaTiSe₄/buffer interface	Ag₂BaTiSe₄/MoSe₂ interface
Defect density	1.0×10^{12} cm^{-3}	1.0×10^{12} cm^{-3}
Defect type	Neutral	Neutral
Capture cross section for electrons	1E−19 cm^2	1E−19 cm^2
Capture cross section for holes	1E−19 cm^2	1E−19 cm^2
Energetic distribution	Single	Single
Reference for defect energy level	Above the highest valence band	Above the highest valence band
Energy level with respect to valence band maximum	0.6 eV	0.6 eV

Table 2. Simulation parameters at the interfaces.

to 10^{20} cm^{-3}), and defect density (10^{12} to 10^{20} cm^{-3}). Further, the material characteristics of novel Ag₂BaTiSe₄ are investigated by tuning its electron affinity, thickness, carrier concentration, and defect density from 4.1 to 4.7 eV, 0.1 to 2 μm, 10^{12} to 10^{18} cm^{-3} and 10^{12} to 10^{20} cm^{-3} respectively. Moreover, the role of MoSe₂'s thickness (0.05–0.2 μm) and carrier concentration (10^{12}–10^{20} cm^{-3}) are analyzed. After that, the impact of defects at the Ag₂BaTiSe₄/MoSe₂ and Ag₂BaTiSe₄/buffer interfaces are examined by varying it from 10^{12} to 10^{20} cm^{-3}. The obtained results corresponding to the different layer parameters are also supported by the C–V, C–F, QE measurements, energy band diagrams, electric field, recombination rates, etc., extracted from SCAPS-1D. Finally, the effect of series resistance (R$_S$), shunt resistance (R$_{Sh}$), and operating temperature are studied for the optimized solar cells.

Results and discussion
Simulation of initial solar cells
The initial solar cells are designed with the solar cell structure of front contact/AZO/IZO/buffers/Ag₂BaTiSe₄/MoSe₂/Mo/Glass as shown in Fig. 1a where new alkaline earth metal chalcogenides such as MgS, CaS, SrS, BaS and conventional CdS are used as buffers. They are simulated using the parameters listed in Tables 1 and 2. The solar cell parameters of the initial solar cells are listed in Table 3, and the corresponding J–V graphs are provided in Fig. 1b. To be brief, initial PCEs of 18.72%, 11.65%, 15.93%, 15.47%, and 14.99% are obtained for MgS, CaS, SrS, BaS, and CdS-based Ag₂BaTiSe₄ solar cells, respectively. The performance of these solar cells is further enhanced by optimizing the material parameters of buffers, Ag₂BaTiSe₄ and MoSe₂, and tuning their interface properties as mentioned in the methodology, which can be seen in the following sections.

Optimization of buffers
The buffer plays a vital role in thin-film solar cells. It develops a p–n junction with the absorber and reduces the pinhole effect and leakage current by terminating the interaction between the absorber and the window layers[62]. Thus, studying their properties to obtain a high PCE is crucial. Therefore, the critical parameters such as thickness, carrier concentration, and defect density of all buffers, namely MgS, CaS, SrS, BaS, and CdS, are varied from 0.05 to 0.2 μm, 10^{12} to 10^{20} cm^{-3}, and 10^{12} to 10^{20} cm^{-3} respectively, to broadly investigate their impact on the performance of solar cells.

Effect of buffer thickness
The thickness of the buffer greatly influences the transportation of electrons from the absorber to the front contact. Therefore, it is crucial to determine the optimum thickness of each buffer to attain maximum solar cell performance. In this regard, we varied the thickness of MgS, CaS, SrS, BaS, and CdS from 0.05 to 0.2 μm, and the respective changes in V$_{OC}$, J$_{SC}$, FF, and PCE are displayed in Fig. 2. The corresponding J–V graphs are given in Fig. S1. It can be observed from Fig. 2a that the V$_{OC}$ of SrS decreases from 1.1 to 0.67 V when the thickness is enhanced from 0.05 to 0.09 μm. The drastic decline may occur due to the reduced quasi-fermi level splitting in SrS-based solar cells with increasing thickness[63]. Nevertheless, it saturates beyond 0.09 μm. The V$_{OC}$ of other buffers remains unaffected, indicating no change in the positions of energy bands and fermi levels in these solar cells corresponding to the buffer thickness[63]. On the other hand, the J$_{SC}$ value increases from 39.27 to 39.38 mA cm^{-2} with an increase in BaS thickness. This is unusual because J$_{SC}$ generally decreases with an increase in buffer

Solar cell structure	V$_{OC}$ (V)	J$_{SC}$ (mA cm^{-2})	FF (%)	PCE (%)
AZO/IZO/MgS/Ag₂BaTiSe₄/MoSe₂/Mo	0.592	39.48	80.03	18.72
AZO/IZO/CaS/Ag₂BaTiSe₄/MoSe₂/Mo	0.488	39.19	60.83	11.65
AZO/IZO/SrS/Ag₂BaTiSe₄/MoSe₂/Mo	0.720	39.45	56.01	15.93
AZO/IZO/BaS/Ag₂BaTiSe₄/MoSe₂/Mo	0.658	39.29	59.75	15.47
AZO/IZO/CdS/Ag₂BaTiSe₄/MoSe₂/Mo	0.569	39.32	66.90	14.99

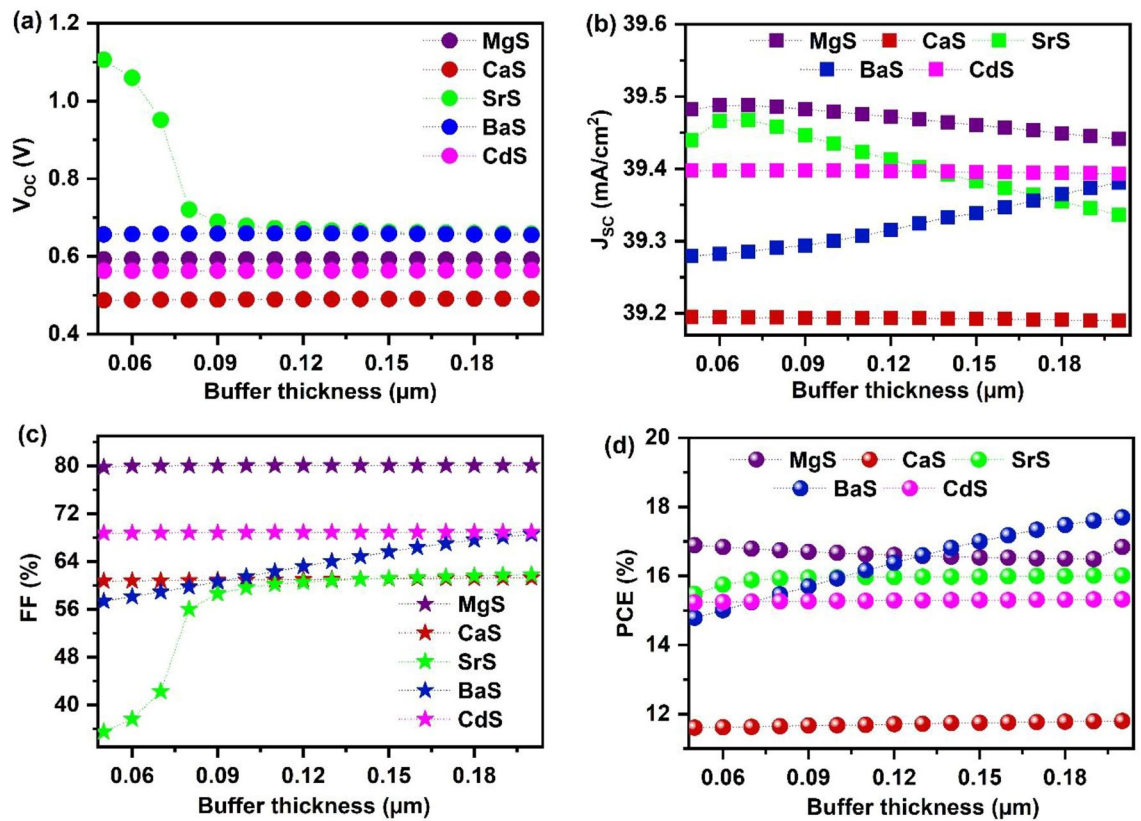**Table 3.** Initial solar cell parameters of novel Ag₂BaTiSe₄ solar cells.

Figure 2. Effect of buffer's thickness on (**a**) V_{OC} (**b**) J_{SC} (**c**) FF (**d**) PCE of novel $Ag_2BaTiSe_4$ based solar cells with diverse buffers.

thickness. It is suspected that this may be due to the characteristics of BaS, and further experimental study is required. In other cases, a small decrease in J_{SC} was observed, which could be attributed to the minute light absorption in buffers and the resulting reduction in charge carrier generation in the absorber[43]. Other researchers have noticed a minor change in J_{SC} due to an increase in buffer thickness, which is considered a constraint in numerical simulations[64–67]. Figure 2c shows that FF significantly increases from 35.47 to 58.64% till 0.09 μm in SrS-based solar cells and improves slightly to 61.8% on further increase to 0.2 μm. Similarly, it also enhances from 79.77 to 80.05%, 60.75 to 61.27%, 57.35 to 68.57%, and 68.71 to 68.93% in MgS, CaS, BaS, and CdS-based solar cells, respectively for the thickness range 0.050 to 0.2 μm. This increment originates from the reduction in the R_S of the solar cells at enhanced buffer thickness[68]. Consequently, PCE also increases in all solar cells (Fig. 2d). However, the improvement is minute, demonstrating that the impact of buffer thickness on the overall performance of all the solar cells is negligible. When making solar cells, the buffer thickness is a critical factor. If it's too thin (below 0.05 μm), it may not cover the entire substrate, causing a high leakage current and a poor p–n junction at the buffer/absorber interface. This, in turn, negatively impacts the spectral response of the solar cell[53,62,69,70]. On the other hand, if the buffer is too thick (over 0.1 μm), it leads to parasitic absorption, reducing the amount of charge carriers that reach the absorber, and reducing the built-in potential at the interface, which makes it harder to generate and collect charge carriers[62,70,71]. To achieve high PCE, it's recommended to use a buffer thickness in the range of 0.05 to 0.1 μm for I_2-II-IV-VI_4 solar cells as found in the literature[16,51,55,58,71]. After considering all these factors, an optimal thickness of 0.080 μm is selected for the alkaline earth metal-based chalcogenide buffers, which falls within the suggested range.

Effect of buffer's carrier concentration and defect density
The buffer's carrier concentration strongly influences the interface properties between the absorber and buffer in solar cells[72]. Thus, to study its influence on solar cell parameters, each buffer's carrier concentration ($N_{D\ buffer}$) is varied from 10^{12} to 10^{20} cm^{-3} while fixing the absorber's carrier concentration ($N_{A\ absorber}$) at 10^{15} cm^{-3} as seen in Fig. 3. The respective J–V graphs are provided in Fig. S1. It can be observed that the V_{OC} of all solar cells stays unaltered till 10^{16} cm^{-3} and slightly increases for CaS and BaS-based solar cells while decreasing for SrS, MgS, and BaS-based solar cells beyond the mentioned value. It is well known that the V_{OC} of the solar cells increases with the splitting of electron and hole quasi-fermi levels, which is produced by the electrochemical potential difference of electrons and holes in each layer of solar cell[73]. In this view, the observed increase or decrease in V_{OC} can be attributed to the increment or reduction in the quasi-fermi level splitting in the respective solar cells with the increasing $N_{D\ buffer}$. On the other hand, J_{SC} and FF values of all solar cells significantly improve above 10^{15} cm^{-3}, leading to improved PCE. When $N_{D\ buffer} > N_{A\ absorber}$, the concentration of electrons at the interface region rises,

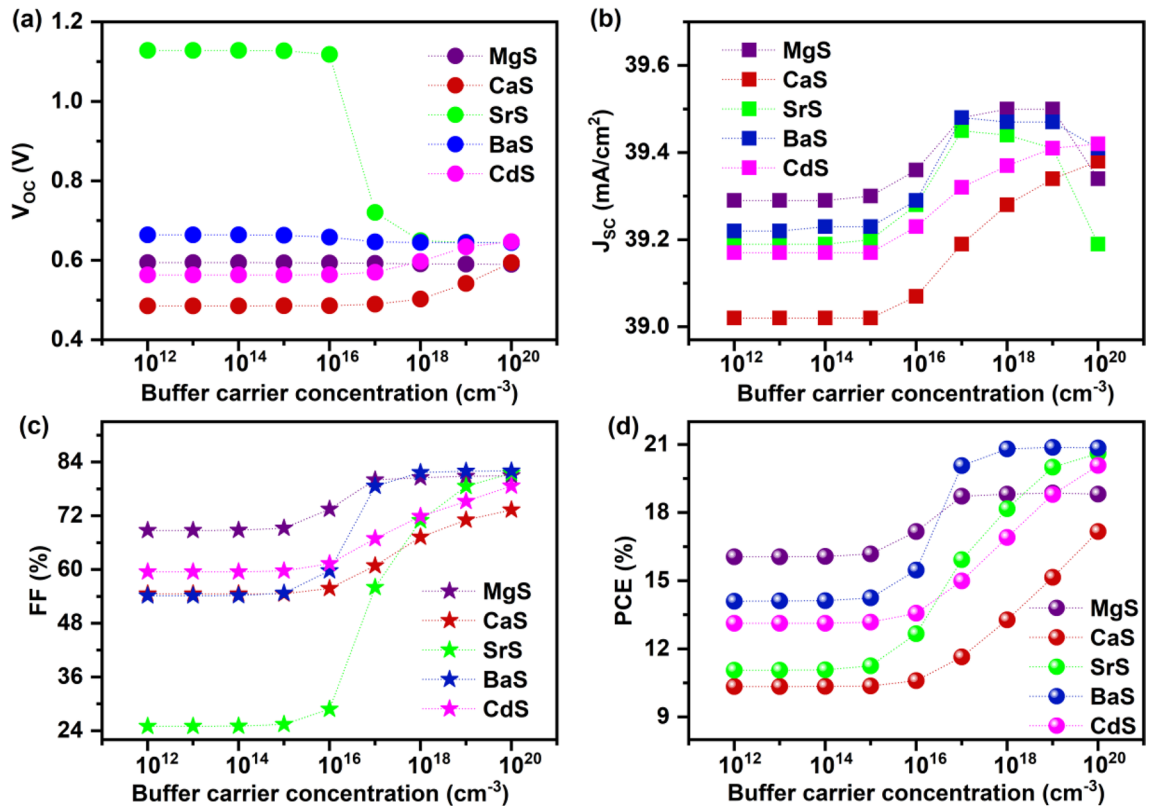**Figure 3.** Effect of buffer's carrier concentration on (**a**) V_{OC} (**b**) J_{SC} (**c**) FF (**d**) PCE of novel Ag$_2$BaTiSe$_4$ solar cells with diverse buffers.

lowering the barrier height at the absorber/buffer interface. This subsequently elevates the built-in potential and conductivity of the solar cells, resulting in enhanced solar cell performance[72]. However, when the $N_{D\,buffer}$ is increased beyond the optimum value, large electron–electron scattering occurs in solar cells, which hinders the carrier transportation, resulting in a slight decrease of J_{SC} and PCE for concentrations above 10^{19} cm^{-3} in MgS and BaS-based solar cells[74]. Thus, an optimum $N_{D\,buffer}$ of 10^{20} cm^{-3} is chosen for CaS, SrS, and CdS buffers, while 10^{19} cm^{-3} is selected for MgS and BaS buffers to obtain the maximum solar cell performance.

In general, $N_{D\,buffer}$ primarily impacts the bending of energy bands at the absorber/buffer interface, facilitating the separation of charge carriers in solar cells[45]. Thus, to attain significant insights into its impact on band bending, the energy band diagram is extracted from SCAPS-1D as a function of $N_{D\,buffer}$, as shown in Fig. 4a–e, where E_C is the conduction band minimum, and E_V is the valence band maximum. It can be seen that when the $N_{D\,buffer}$ is less than or equal to the $N_{A\,absorber}$, no change is observed in the band alignment, attributing to the unaltered solar cell performance till 10^{15} cm^{-3}. In addition, the barrier for electrons at the absorber/buffer and buffer/IZO interface is large. On the contrary, as the $N_{D\,buffer}$ increases above the $N_{A\,absorber}$, the E_C and E_V of the buffer move downwards, reducing the barrier at both interfaces and boosting the transport efficiency of charge carriers. This occurs because, at $N_{D\,buffer} < N_{A\,absorber}$, the holes primarily occupy the absorber/buffer interface energy states, which act as a recombination center for the photogenerated electron, impeding its flow towards respective contact[72]. Moreover, as the electron concentration at the interface is very low, a large spike is formed at the absorber/buffer interface[75]. Nevertheless, for $N_{D\,buffer} > N_{A\,absorber}$, the electrons predominantly occupy the lower density of states in the buffer's conduction band and near interface states of absorber/buffer junction. This eventually improves the interaction and exchange potential between the charge carriers, resulting in a downward shift of energy bands. As a result, the barriers at the absorber/buffer and buffer/IZO interface shrink, enhancing the conductivity of the solar cells[45,76]. Furthermore, it could be noticed that the bending of buffer's E_C and E_V is large in MgS, SrS, and BaS-based solar cells while it is less in CaS and CdS-based solar cells. This reveals that the influence of $N_{D\,buffer}$ on the band bending of CaS and CdS-based solar cells is comparatively smaller than MgS, SrS, and BaS-based solar cells.

Impedance spectroscopy is a vital characterization technique to investigate the accumulation of charge carriers at the interface in solar cells[77]. Therefore, C–V measurements are performed between 10^{12} cm^{-3} and the optimum $N_{D\,buffer}$ of each solar cell to analyze the accumulation of charge carriers at the absorber/buffer interface (Fig. 4f–j). All measurements are executed at 1 MHz frequency to address the repercussions of deep-level defects. From the C–V plots of all solar cells, it can be observed that the capacitance remains constant and has less values at lower voltages, corresponding to the depletion capacitance (C_{DEP}), which originates from the depletion region at the absorber/buffer junction. Conversely, it is comparatively large at higher voltages. This behavior occurs because the depletion region shrinks as the voltage increases, resulting in a large accumulation of charge carriers at the interface. As a consequence, capacitance increases, which is termed as accumulation capacitance (C_{ACC})[78]. It
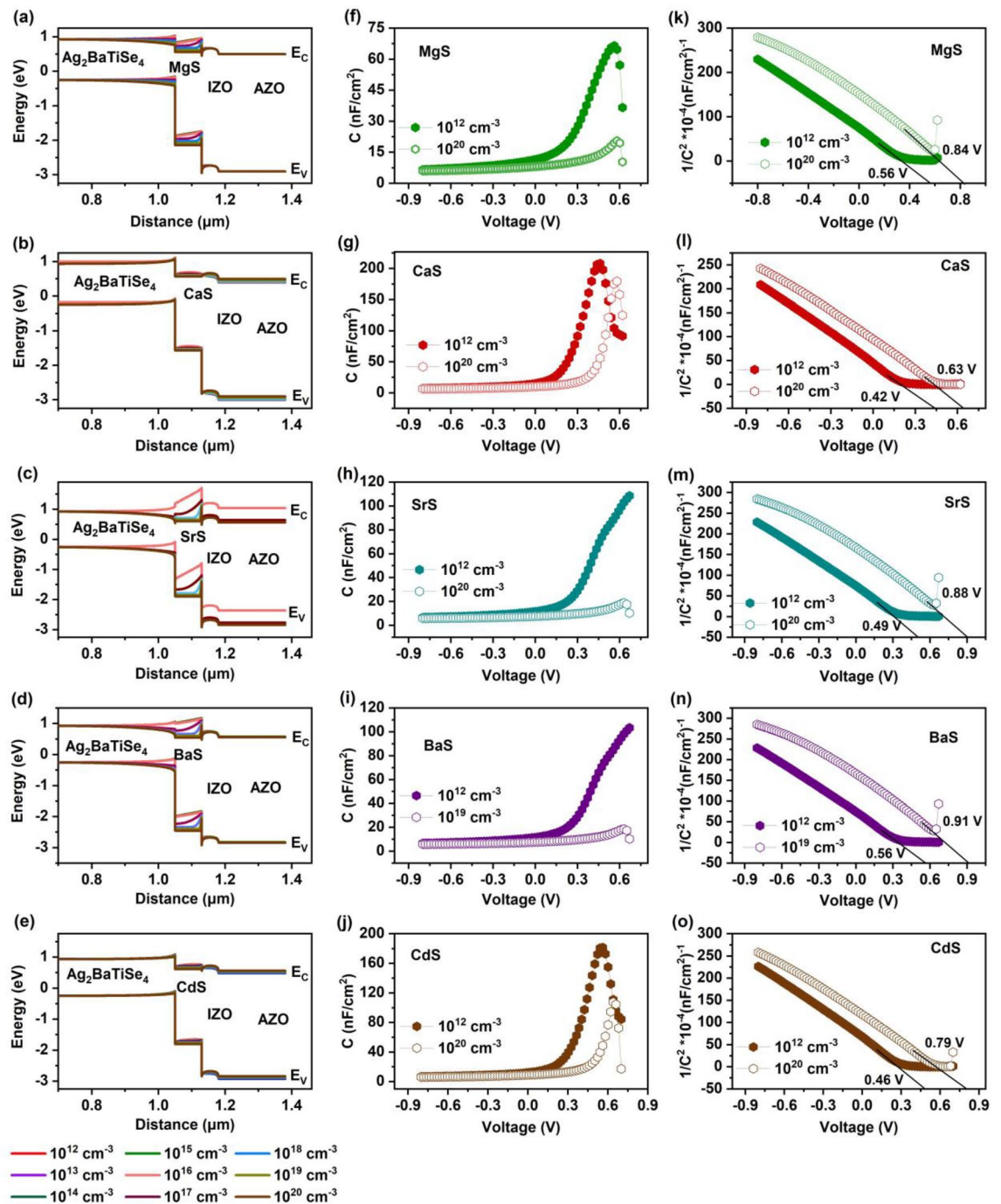
Figure 4. (**a-e**) Variation in energy band diagram of novel $Ag_2BaTiSe_4$ solar cells with diverse buffers as a function of $N_{D\ buffer}$. (**f–j**) C–V and (**k–o**) Mott-Schottky plots with corresponding V_b at 10^{12} cm^{-3} and optimized $N_{D\ buffer}$.

can be noticed in Fig. 4f–j that the C_{ACC} of all solar cells at 10^{12} cm^{-3} is very high compared to the optimized $N_{D\ buffer}$, denoting that the accumulation of charge carriers at the interfaces is intense at 10^{12} cm^{-3}, which boosts the recombination in the bulk region. This is also evident in Fig. 4a–e, where the barrier for electrons at the $Ag_2BaTiSe_4$/buffer interface is large at 10^{12} cm^{-3}. Thus, the photogenerated electrons in the absorber require more energy to cross the barriers and get collected at the front contact. As a result, they accumulate in the absorber and eventually recombine with the holes. Whereas, at an optimized $N_{D\ buffer}$, the possibility for charge carrier accumulation decreases due to the reduction in the barrier, resulting in a fast collection of charge carriers without recombination. This has led to improved solar cell performance at an optimized $N_{D\ buffer}$. Furthermore, in the C–V plot, we could notice that the voltage at which the capacitance begins to rise, shifts to a higher voltage for optimized $N_{D\ buffer}$ in all solar cells. In other words, it can be said that C_{DEP} extends to higher voltage when the $N_{D\ buffer}$ is increased, revealing that the depletion width at the p–n junction has been improved at a higher

$N_{D\ buffer}$. To witness it, the Mott Schottky ($1/C^2$) graph is plotted from the C–V, and the built-in potential (V_b) is determined from the intercept of the plot. It is clear from Fig. 4k–o that V_b has been drastically improved from 0.56 to 0.84 V, 0.42 to 0.63 V, 0.49 to 0.88 V, 0.56 to 0.91 V, 0.46 to 0.79 V for MgS, CaS, SrS, BaS, and CdS-based solar cells respectively, after optimizing the $N_{D\ buffer}$. The corresponding depletion width (W) of each solar cell was calculated using the following equation[79]:

$$\text{Depletion width} = \sqrt[2]{\frac{2\varepsilon_0\varepsilon_S V_b}{qN_{A\ absorber}}} \tag{6}$$

where ε_0 is the dielectric permittivity of free space, ε_S is the dielectric constant, and q is the elementary charge. At 10^{12} cm^{-3}, W is deduced to be 0.61 μm, 0.51 μm, 0.57 μm, 0.60 μm and 0.55 μm for MgS, CaS, SrS, BaS, and CdS-based solar cells respectively and improved to 0.74 μm, 0.64 μm, 0.76 μm, 0.77 μm and 0.72 μm at optimized $N_{D\ buffer}$. It is essential to highlight that the W will extend towards the absorber as $N_{D\ buffer} > N_{A\ absorber}$. Since most of the light absorption and charge carrier generation occurs in the depletion region along the absorber side, the increase in W boosts the amount of carrier generation in solar cells. Moreover, the elevation in V_b would hasten the charge carrier separation and improve their collection at the respective contacts[62]. Thus, final PCE of 18.81%, 17.17%, 20.6%, 20.85%, and 20.08% are obtained for MgS, CaS, SrS, BaS, and CdS-based solar cells, respectively, at the optimized $N_{D\ buffer}$. The discussed research findings reveal $N_{D\ buffer}$'s dominant role in enhancing solar cell performance.

After that, the effect of defect density of each buffer is investigated by tuning it from 10^{12} to 10^{20} cm^{-3} (Fig. 5). The corresponding J–V graph is given in Fig. S1. All the photovoltaic parameters remain almost constant up to a specific range in all solar cells and slightly decrease to lower values with further increase in defects. In particular, PCE reduced from 18.86 to 18.3%, 17.17 to 15.61%, 20.63 to 19.87%, 20.9 to 20.49%, 18.69 to 17.72% for MgS, CaS, SrS, BaS, and CdS-based solar cells respectively, when the defect density is increased from 10^{12} to 10^{20} cm^{-3}. The reduction in solar cell performance occurs because the rise in the defect states acts as traps for the charge carriers, which boosts the recombination rate in solar cells[80]. However, it can be noticed that the level of decrement is small, i.e., 0.56%, 1.56%, 0.76%, 0.41%, and 0.97% for MgS, CaS, SrS, BaS, and CdS-based solar cells. This indicates that the influence of the buffer's defect density on the solar cell performance is negligible. Based on the results, an optimum defect density of 10^{16} cm^{-3} for MgS, 10^{15} cm^{-3} for BaS and SrS, and 10^{17} cm^{-3} for CdS and CaS are selected for further simulations.
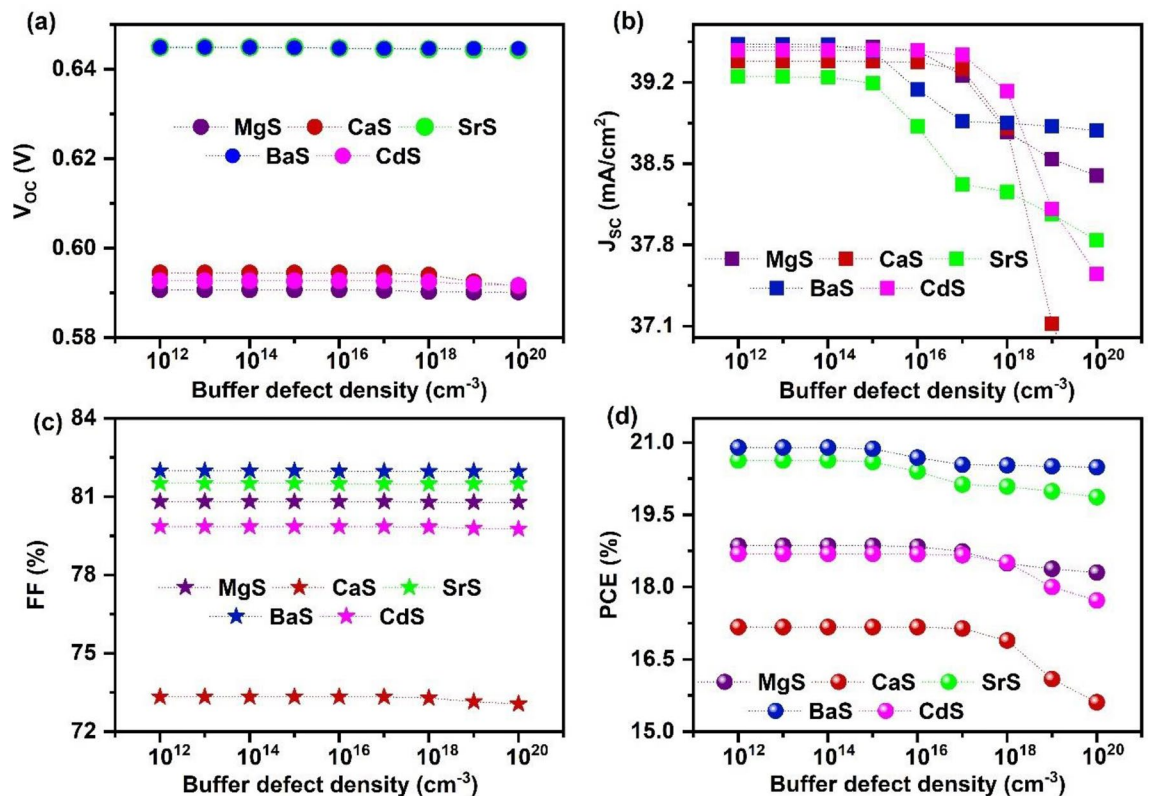

Figure 5. Effect of buffer's defect density on (**a**) V_{OC} (**b**) J_{SC} (**c**) FF (**d**) PCE of novel Ag$_2$BaTiSe$_4$ solar cells with diverse buffers.

Absorber optimization

The absorber is the most critical layer in solar cells, as most charge carriers are generated here. Thus, the quality of the absorber is crucial to attain maximum solar cell performance. Therefore, the material parameters of $Ag_2BaTiSe_4$, such as electron affinity, thickness, carrier concentration, and defect density, are varied from 4.1 to 4.7 eV, 0.1 to 2 μm, 10^{12} to 10^{18} cm^{-3} and 10^{12} to 10^{20} cm^{-3} respectively to understand their influence on the solar cell performance. The results of the $Ag_2BaTiSe_4$ optimization are elucidated in the following sections.

Effect of absorber's electron affinity

Adjusting the energy band offsets at the absorber/buffer and $MoSe_2$/absorber interface is essential to alleviate the formation of energy barriers and enhance the collection of charge carriers in solar cells[81]. This can be directly achieved by tuning the electron affinity of the absorber as it governs the energy band offsets at both interfaces. Herein, the electron affinity of $Ag_2BaTiSe_4$ is varied from 4.1 to 4.7 eV to identify the optimum energy band offset values in all solar cells. The variation in photovoltaic parameters as a function of electron affinity is displayed in Fig. 6a–d, and the corresponding J–V graphs are given in Fig. S2. The V_{OC} of all solar cells increases till 4.6 eV and reduces at 4.7 eV, while J_{SC} remains constant throughout the affinity range in all the solar cells except for SrS-based solar cells, where it drastically decreases after 4.6 eV. On the other hand, FF and PCE follow the same trend in all solar cells, and their maximum values are demonstrated at 4.4 eV. The affinity values above or below 4.4 eV degrade the solar cell performance. The obtained results can be clearly understood in light of variations in energy band offsets concerning the absorber's electron affinity. High conduction band offset (CBO) and low valence band offset (VBO) are generally required at the $MoSe_2$/absorber interface to restrict electrons and efficiently transport the photogenerated holes. Low CBO and high VBO are essential at the absorber/buffer interface to effectively collect electrons at the front contact[82]. Hence, CBO and VBO at both interfaces corresponding to each affinity value of absorber is calculated using the following formula[83]:

Absorber/buffer interface

$$CBO = \chi_{absorber} - \chi_{buffer} \tag{7}$$

$$VBO = [E_{G\ buffer} + \chi_{buffer}] - [E_{G\ absorber} + \chi_{absorber}] \tag{8}$$

$MoSe_2$/absorber interface

$$CBO = \chi_{absorber} - \chi_{MoSe_2} \tag{9}$$

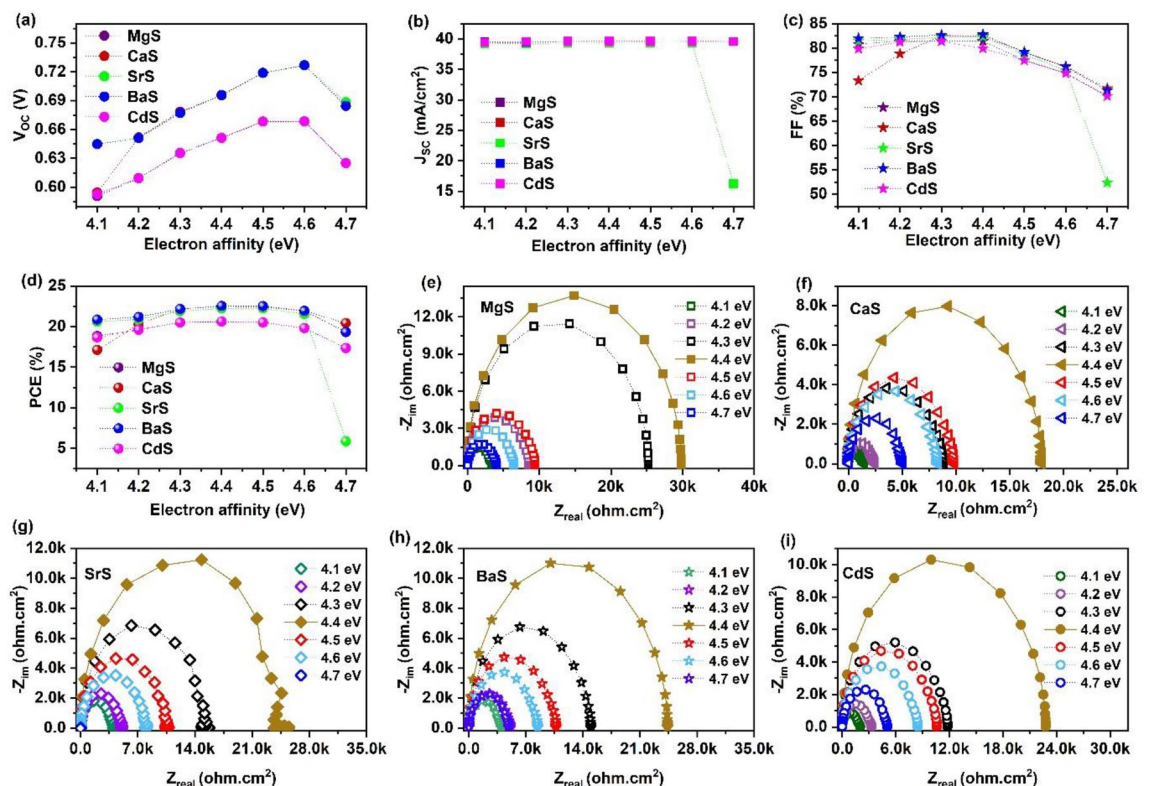$$VBO = [E_{G\ MoSe_2} + \chi_{MoSe_2}] - [E_{G\ absorber} + \chi_{absorber}] \tag{10}$$

Figure 6. Effect of absorber's electron affinity on (**a**) V_{OC} (**b**) J_{SC} (**c**) FF (**d**) PCE of novel $Ag_2BaTiSe_4$ solar cells with diverse buffers, (**e–i**) Nyquist plots as a function of absorber's electron affinity.

where χ_{MoSe_2}, χ_{buffer}, $\chi_{absorber}$ and $E_{G\ MoSe_2}$, $E_{G\ buffer}$, $E_{G\ absorber}$ are the affinity and bandgap of MoSe$_2$, buffer, and absorber respectively. The calculated CBO and VBO of all solar cells at both interfaces are explicitly provided in Table 4. On analyzing the MoSe$_2$/absorber interface, VBO holds positive and negative values with the absorber's electron affinity variation. At positive VBO, a spike is created at the MoSe$_2$/absorber interface, which hinders the diffusion of holes from the absorber to MoSe$_2$. In the case of negative VBO, the photogenerated holes in the absorber have a cliff-like barrier that boosts the collection of holes at the back contact. However, a large cliff elevates the accumulation of holes in MoSe$_2$, which enhances the recombination at the back contact, deteriorating the solar cell performance[84]. Thus, the optimum VBO at the MoSe$_2$/absorber interface is identified to be -0.06 eV to demonstrate maximum PCE. Similarly, two conditions are observed at the absorber/buffer interface[84]: (1) When the affinity of the absorber is less than the buffer, negative CBO is obtained, representing cliff formation. (2) Positive CBO is attained when it is higher than the buffer, leading to spike formation at the interface.

It has been commonly believed for a long time that a cliff at the absorber/buffer interface is beneficial for solar cells, as the separation and extraction of the charge carriers are not constrained while it is restricted by spikes due to the formation of barrier at the interface[85]. Later, the development of simulation tools and experimental results proved that a moderate spike-like barrier is also advantageous for solar cells as it creates strong V$_b$ at the interface, enhancing the carrier collection at the contacts[86,87]. Moreover, in some cases, a large cliff-like barrier has also been observed, which leads to charge carrier accumulation at the interface due to the weak potential barrier, improving the interfacial recombination and thereby affecting the solar cell performance[88]. Thus, it is important to mention that the ideal type of barrier (either spike or cliff) required at the absorber/buffer interface and optimum values of the barrier height in solar cells are scattered in the literature, revealing that it primarily depends on the adopted material system[75,87,89]. The results show that CaS, CdS-based solar cells require a cliff-like barrier with a height of -0.2 eV and -0.1 eV to attain maximum solar cell performance. Whereas the spikes of 0.1 eV, 0.4 eV, and 0.25 eV are essential in MgS, SrS, and BaS-based solar cells. The positive or negative CBO above or below the mentioned values would degrade the solar cell performance due to the unfavorable band alignment at the absorber/buffer interface. Furthermore, the obtained results exhibit that the difference in the type of barrier and their respective barrier height mainly stems from the material characteristics of the buffer, as the other layers in these solar cells are similar, revealing the dominant role of buffer properties for the efficient transportation of charge carriers. It has also been reported elsewhere that buffer's parameters, such as carrier concentration, the effective density of states, interface defect states, etc., determine the barrier height at the interface, thus confirming the demonstrated results[75]. Moreover, the optimum VBO and CBO calculated at the absorber/buffer and MoSe$_2$/absorber interface, respectively, are also ideal for restricting the holes and electrons in the respective interfaces. Hence, the electron affinity of 4.4 eV is required in Ag$_2$BaTiSe$_4$ to achieve high PCE.

In addition, to gain a deep understanding of the variations in the transportation and recombination of charge carriers corresponding to the absorber's electron affinity, Nyquist plots are plotted from C-F measurements in all solar cells, as shown in Fig. 6e–i. Generally, the Nyquist plot of solar cells consists of two semi-circles at separate frequency regions. The semi-circle at the low-frequency range denotes the recombination resistance (R$_{rec}$) at the absorber/buffer interface, while the high-frequency semicircle signifies the hole transfer resistance at the MoSe$_2$/absorber interface[90]. Interestingly, a single semi-circle is observed in all these solar cells in the whole frequency range. In addition, the semicircle obtained at the optimum electron affinity, i.e., 4.4 eV, is larger than the other affinity values in all solar cells. This indicates that the obtained semicircle represents the R$_{rec}$. The absence of high-frequency semicircles reveals no hole transfer resistance in these solar cells. As discussed above, the large semicircle at 4.4 eV displays that the solar cells have high R$_{rec}$ at the optimum electron affinity, occurring due to the proper CBO and VBO at the interfaces of the absorber and transporting layers. The shrinkage in the semicircle for the affinity values above or below 4.4 eV happens due to the surging recombination rate of charge carriers resulting from improper interface barriers. From the above discussions, it is apparent that proper CBO and VBO at the absorber/buffer and MoSe$_2$/absorber interface are essential to effectively transport the photogenerated charge carriers to the contacts without recombination.

Effect of absorber's thickness
The thickness of the absorber plays a vital role in understanding the performance of solar cells. Thus, the thickness of Ag$_2$BaTiSe$_4$ is varied from 0.1 to 2 μm to identify the optimum value. Figure 7a–d displays the variations in

| Affinity (eV) | Absorber/buffer interface | | | | | | | | | | Absorber/MoSe$_2$ interface | |
| | MgS | | SrS | | BaS | | CaS | | CdS | | | |
	CBO (eV)	VBO (eV)	CBO (eV)	VBO (eV)	CBO (eV)	VBO (eV)	CBO (eV)	VBO (eV)	CBO (eV)	VBO (eV)	CBO (eV)	VBO (eV)
4.1	-0.2	1.72	0.1	1.22	-0.05	1.87	-0.5	1.46	-0.4	1.64	-0.02	0.24
4.2	-0.1	1.62	0.2	1.12	0.05	1.77	-0.4	1.36	-0.3	1.54	0.08	0.14
4.3	0	1.52	0.3	1.02	0.15	1.67	-0.3	1.26	-0.2	1.44	0.18	0.04
4.4	**0.1**	**1.42**	**0.4**	**0.92**	**0.25**	**1.57**	**-0.2**	**1.16**	**-0.1**	**1.34**	**0.28**	**-0.06**
4.5	0.2	1.32	0.5	0.82	0.35	1.47	-0.1	1.06	0	1.24	0.38	-0.16
4.6	0.3	1.22	0.6	0.72	0.45	1.37	0	0.96	0.1	1.14	0.48	-0.26
4.7	0.4	1.12	0.7	0.62	0.55	1.27	0.1	0.86	0.2	1.04	0.58	-0.36

Table 4. Electron affinity of absorber with the corresponding CBO and VBO at the interfaces of novel Ag$_2$BaTiSe$_4$ solar cells with diverse buffers. Optimum values are in [bold].
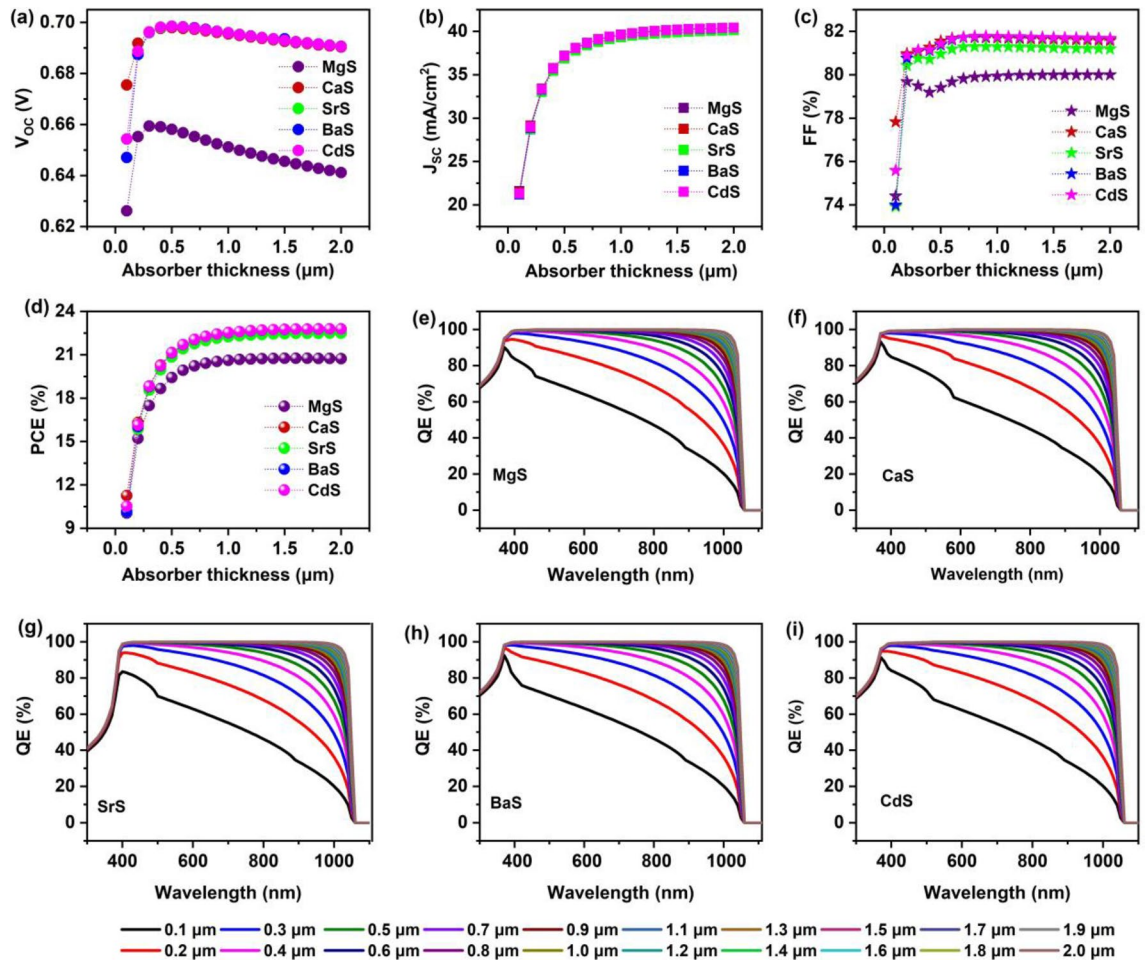
Figure 7. Effect of absorber's thickness on (**a**) V_{OC} (**b**) J_{SC} (**c**) FF (**d**) PCE (**e-i**) QE of novel $Ag_2BaTiSe_4$ solar cells with diverse buffers.

V_{OC}, J_{SC}, FF, and PCE as a function of absorber thickness. The respective J–V graphs are given in Fig. S2. It can be noticed that the V_{OC} of all solar cells improves till ∼ 0.3 μm and slightly decreases after the mentioned value. The initial improvement is attributed to enhanced quasi-fermi level splitting with the large generation of charge carriers whereas its reduction originates from the elevating dark saturation current and recombination rate with the thickness[91]. In addition, FF rises till a certain thickness range and saturates in all the solar cells, occurring due to the enhanced R_S in a solar cell for thicker absorber[91]. On the other hand, when the thickness is increased from 0.1 to 2 μm, J_{SC} drastically improves from ∼ 21 to ∼ 40 mA cm⁻² in all solar cells. This has subsequently elevated PCE from 10.05 to 20.74%, 11.27 to 22.75%, 10.13 to 22.75%, 10.13 to 22.5%, 10.15 to 22.79%, and 10.54 to 22.79% in MgS, CaS, SrS, BaS and CdS-based solar cells respectively. This happens because when the absorber is very thin, photons of longer wavelengths from the sun are not absorbed, and most of the light is transmitted. This results in the poor generation of charge carriers in solar cells due to low performance. As the thickness increases, the photon absorption in solar cells is enhanced, elevating the generation rate of charge carriers[92]. This has led to a steep rise in solar cell performance. However, we could see that J_{SC} significantly improves till 1 μm and saturates beyond the mentioned value. A similar trend has also been observed in PCE. In particular, when the thickness is enhanced from 0.1 to 1 μm, the increment in PCE is about 10.57%, 11.23%, 12.12%, 12.38%, and 12% for MgS, CaS, SrS, BaS, and CdS-based solar cells respectively. While it increased by just ∼ 0.25% in all the solar cells when the thickness was extended 1–2 μm. When the absorber is too thick, the generated charge carriers must travel long distances to reach the respective contacts. Thus, the majority of them tend to recombine due to shorter diffusion lengths than the absorber thickness, causing saturated solar cell performance[93]. This is also evident in QE measurements (Fig. 7e–i), where the absorption increases by ∼ 34% in all the solar cells for the thickness range of 0.1 to 1 μm. Whereas it improves by ∼ 1.5% on further increment to 2 μm. In I_2-II-IV-VI_4 solar cells, experiments have shown that an absorber thickness of approximately 1 μm is ideal for majority photon absorption due to its high absorption coefficient (∼ 10⁵ cm⁻¹)[54,94–96]. For example, when the thickness of CZTS was adjusted from 0.5 to 2 μm, the PCE gradually increased up to 1 μm and then stabilized beyond that. QE measurements revealed that the collection depth of minority carriers ranged from 0.75 to 1 μm, indicating that recombination was high for thicknesses greater than 1 μm. Conversely, for absorber thicknesses less than 0.75 μm, there were high collection losses of charge carriers in the solar cells. Therefore, the optimal thickness

for the CZTS absorber was determined to be around 1 µm for achieving high PCE[97]. Our simulation results were compared with the experiments, and we concluded that a thickness of 1 µm for $Ag_2BaTiSe_4$ would be sufficient to achieve high solar cell performance.

Effect of absorber's carrier concentration

The $N_{A\ absorber}$ modifies its electrical conductivity and determines the charge separation efficiency of the solar cells[98]. According to the Mott criterion, the maximum carrier concentration limit of CZTS is 10^{18} cm^{-3}. Beyond this, it degenerates and loses its semiconducting property, adversely affecting the J_{SC} of solar cells[99]. Thus, taking insights from the parent material, the carrier concentration of $Ag_2BaTiSe_4$ is varied from 10^{12} to 10^{18} cm^{-3} in all solar cells. The changes in the solar cell parameters concerning the $N_{A\ absorber}$ are displayed in Fig. 8. The J–V graphs are provided in Fig. S3. It can be seen that the V_{OC} and FF of all solar cells are unchanged till 10^{14} cm^{-3}, and then it drastically increases with the $N_{A\ absorber}$.

In general, the improvement in the $N_{A\ absorber}$ amplifies the V_b at the interface, promoting the separation efficiency of photogenerated charge carriers[100]. Mott-Schottky plots for 10^{12} and 10^{18} cm^{-3} and their corresponding V_b are shown in Fig. 9a–e. When $N_{A\ absorber}$ is 10^{12} cm^{-3}, V_b of MgS, CaS, SrS, BaS, and CdS-based solar cells are identified to be 0.54 V, 0.61 V, 0.6 V, 0.59 V and 0.64 V respectively which are then increased to 0.9 V, 0.95 V, 1.01 V, 1.03 V and 1.18 V at 10^{18} cm^{-3}. Thus, the attained increment in V_b assists in efficiently separating and collecting the generated charge carriers at the respective electrodes without recombination, leading to a drastic rise in V_{OC} and FF. In addition, the increase in $N_{A\ absorber}$ modifies the energy band alignment and enhances the quasi-fermi level splitting, boosting the V_{OC} and overall performance of solar cells. Therefore, to witness it, energy band diagrams for 10^{12} and 10^{18} cm^{-3} are extracted from SCAPS-1D in all solar cells (Fig. 9f–j). When N_A is increased from 10^{12} to 10^{18} cm^{-3}, the energy bands of all the layers in the solar cell shift upwards, such that the E_V of the absorber moves closer to the hole quasi-fermi level (F_P). This strongly elevates the conductivity of solar cells, leading to improved solar cell performance. Notably, no change is observed in the position of F_P along $Ag_2BaTiSe_4$ and $MoSe_2$, whereas the electron quasi-fermi level (F_N) shifts upward along with the energy bands with increasing $N_{A\ absorber}$, disclosing the increment in the splitting of quasi-fermi levels, which directly improves the V_{OC} of solar cells. Contrastingly, J_{SC} remains constant till 10^{15} cm^{-3} and decreases with a further increase in the $N_{A\ absorber}$. This happens because as the $N_{A\ absorber}$ increases, the width of the depletion region decreases along the absorber region while improving towards the buffer, which reduces the light absorption in solar cells[45]. This can also be evidenced in Fig. 9k–o, where QE is performed between 10^{12} and 10^{18} cm^{-3} in all solar cells. The absorption slightly decreases by 1.18%, 1.14%, 1.2%, 1.17%, and 1.16% in MgS, CaS, SrS, BaS, and CdS-based solar cells, causing a reduction in J_{SC}. In addition, the possibility of charge carrier generation in the quasi-neutral region of the absorber increases with a decrement of W in the absorber, and the charge carriers
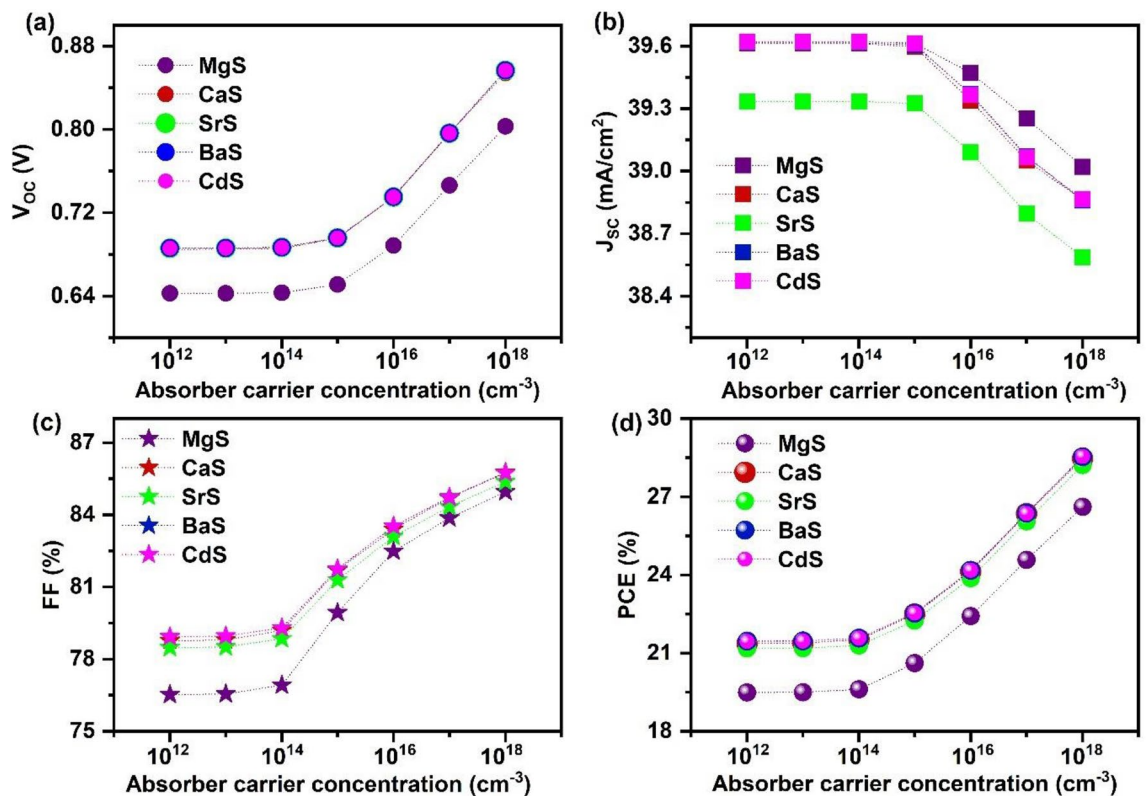

Figure 8. Effect of absorber's carrier concentration on (**a**) V_{OC} (**b**) J_{SC} (**c**) FF (**d**) PCE of novel $Ag_2BaTiSe_4$ solar cells with diverse buffers.
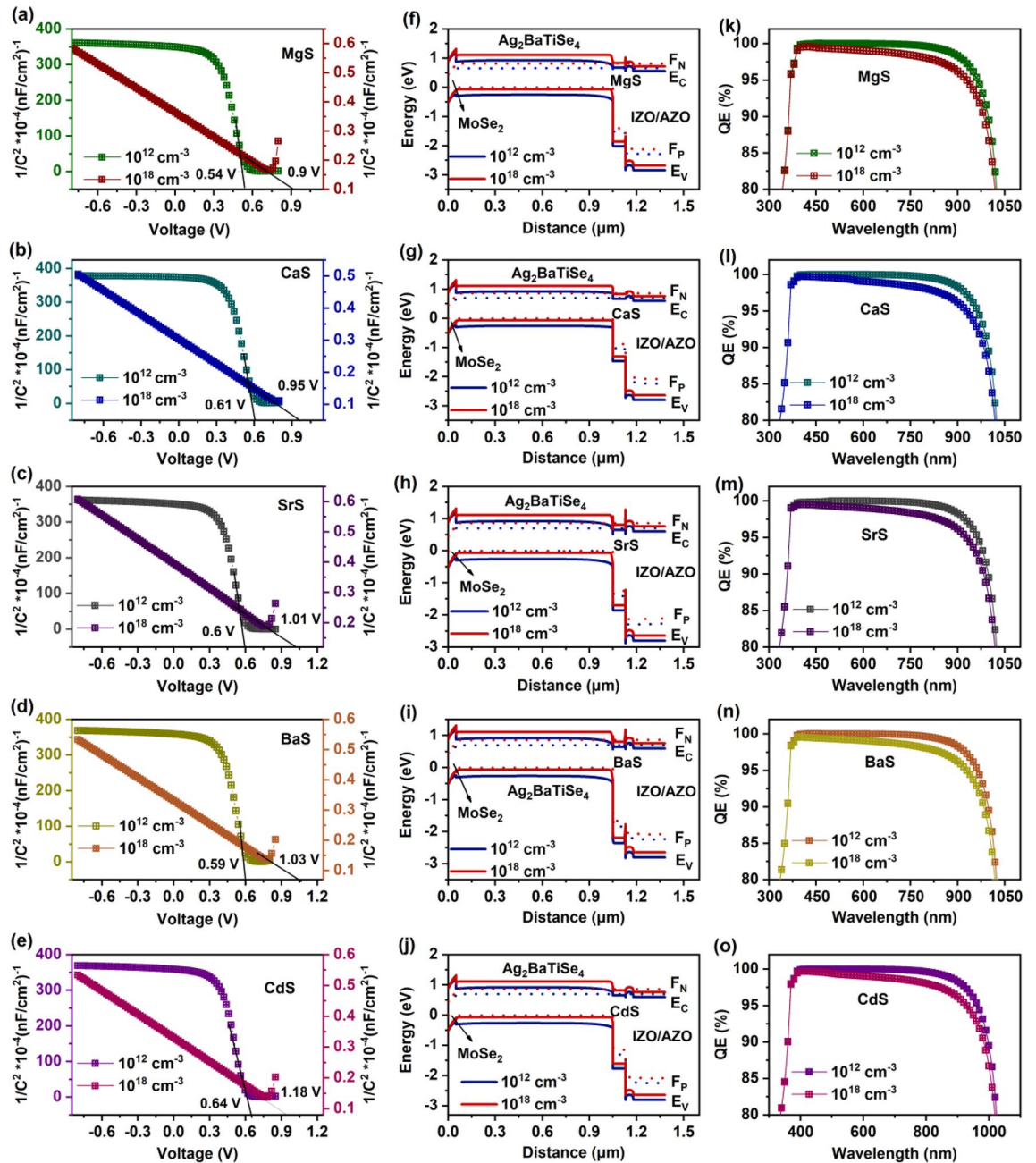
Figure 9. (**a–e**) Mott-Schottky plots with respective V_b, (**f–j**) Energy band diagram and (**k–o**) Changes in QE (magnified image) at absorber's carrier concentration of 10^{12} and 10^{18} cm^{-3} in novel Ag$_2$BaTiSe$_4$ solar cells with diverse buffers. The simplified illustration of QE is provided in Fig. S4.

generated far from the junction have to diffuse through W to reach the contacts. Some of them with insufficient diffusion length and lifetime may recombine, diminishing the J_{SC} of solar cells[100]. However, when the $N_{A\ absorber}$ is increased from 10^{12} to 10^{18} cm^{-3}, PCE drastically rises from 19.49 to 26.62%, 21.37 to 28.47%, 21.18 to 28.22%, 21.46 to 28.54% and 21.45 to 28.55% for MgS, CaS, SrS, BaS, and CdS-based solar cells respectively which mainly comes from the combined improvement of V_{OC} and FF values while the demise in J_{SC} does not affect the overall performance of the solar cells.

Effect of absorber's defect density
The optoelectronic properties of solar cells are adversely affected by defects in the material system[81]. Therefore, the influence of the absorber's defect density on the photovoltaic parameters is examined by tuning it from 10^{12} to 10^{20} cm^{-3} in all solar cells. Figure 10a–d shows the changes in V_{OC}, J_{SC}, FF, and PCE as a function of absorber defect density, and the respective J–V is displayed in Fig. S3. All the solar cell parameters are almost unaltered till 10^{15} cm^{-3} and dramatically falls on further increase in defect density. To be specific, when defect density is
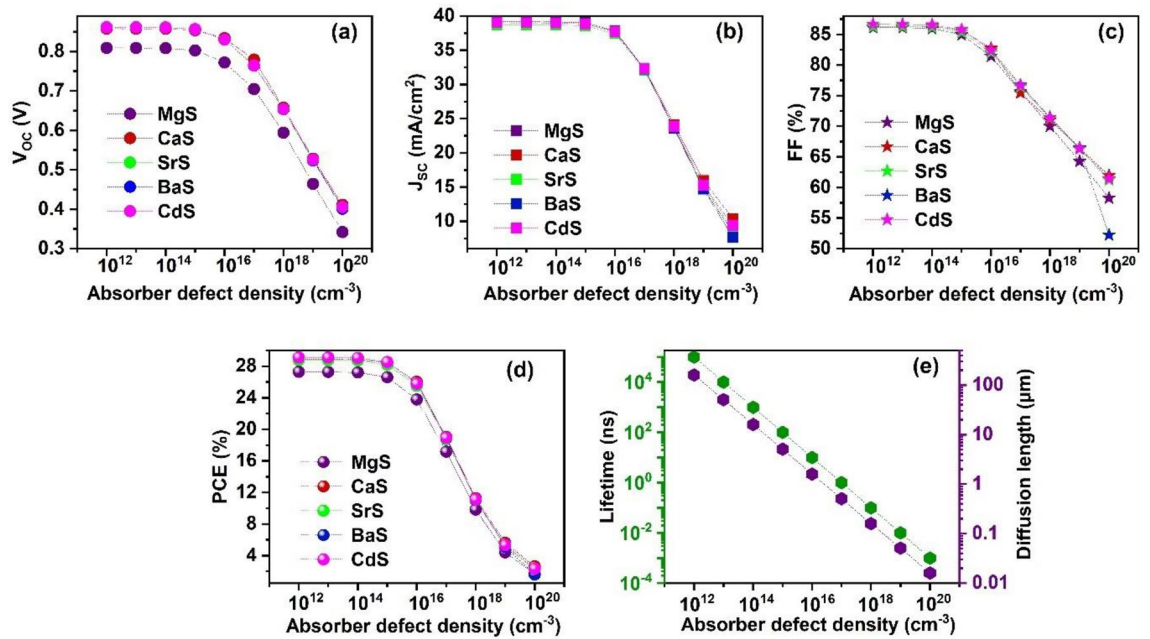
Figure 10. Effect of absorber's defect density on (**a**) V_{OC} (**b**) J_{SC} (**c**) FF (**d**) PCE and (**e**) diffusion length and lifetime of charge carriers of novel $Ag_2BaTiSe_4$ solar cells with diverse buffers.

improved from 10^{12} to 10^{20} cm^{-3}, PCE sharply declines from 27.3 to 1.68%, 28.9 to 2.64%, 28.8 to 2.22%, 29.13 to 1.6% and 29.13 to 2.33% for MgS, CaS, SrS, BaS, and CdS-based solar cells respectively. The massive decline occurs due to the increase in the recombination sites at the path of photogenerated charge carriers with increasing defects, which shortens their diffusion length and lifetime[101]. Generally, the minority carrier lifetime (τ) is calculated using Eq. (11)[102]

$$\tau = \frac{1}{\sigma v_{th} N_t} \tag{11}$$

Here σ is the capture cross-section of the charge carrier, v_{th} is the thermal velocity, and N_t is the defect density. The diffusion length of charge carriers is given as

$$L = \sqrt{D\tau} \tag{12}$$

where L is the minority carrier diffusion length and D is the diffusion coefficient. Herein, the L and τ are acquired from SCAPS-1D for the varying defect density of the absorber with a thickness of 1 μm (Fig. 10e). When the defect density is raised from 10^{12} to 10^{20} cm^{-3}, the τ considerably decreased from 10^5 to 10^{-3} ns and their L drastically reduced from 160 μm to 0.016 μm. On comparing the obtained solar cell parameters with Fig. 10e, it can be observed that the PCE almost remains unaffected till L of 5.1 μm, slightly decreases for L = 1.6 μm while firmly falls for L ≥ 0.5 μm, confirming that L less than the thickness of the absorber adversely affects the solar cell performance. Moreover, the observed decrement in L and τ elevates the recombination rate of charge carriers, leading to poor solar cell performance.

The recombination rate concerning the increasing defect density in all solar cells is shown in Fig. 11a–e. As the defect density increases, the recombination rate shoots up in the absorber region near the absorber/buffer junction of all solar cells, giving rise to deterioration in solar cell performance. Interestingly, the recombination at the absorber/MoSe$_2$ interface decreases with defect density. This occurs because, as the recombination in the absorber region increases, the density of photogenerated carriers drastically reduces in the entire bulk region of the absorber and the near interface regions. This subsequently declines the number of charge carriers reaching the electrodes, reducing the recombination rate at the absorber/MoSe$_2$ interface. This is also evident from Fig. 11f–j where the variation in density of minority carriers (electrons 'n') in the absorber region for the defect density 10^{12} and 10^{20} cm^{-3} of all solar cells are explicitly displayed. It can be seen that the density of electrons in the absorber region becomes negligible at 10^{20} cm^{-3}, resulting from the hiking recombination rate in the absorber. In addition, electrons at the absorber/buffer interface of MgS, SrS, and BaS-based solar cells are diminished at 10^{20} cm^{-3}, indicating that there is sharp recombination at the absorber/buffer interface of these solar cells as witnessed in Fig. 11a, c, d. Furthermore, the electric field at the interface of the absorber and buffer is minimized with increasing defects, as shown in Fig. 11k–o. Thus, the separation and collection of charge carriers are considerably affected, worsening the performance of solar cells. Overall, the results show that the defect density rise greatly affects the L and τ of charge carriers, increasing the recombination rate in solar cells. Consequently, the density of minority carriers and built-in electric field at the p–n junction declined, drastically reducing the solar
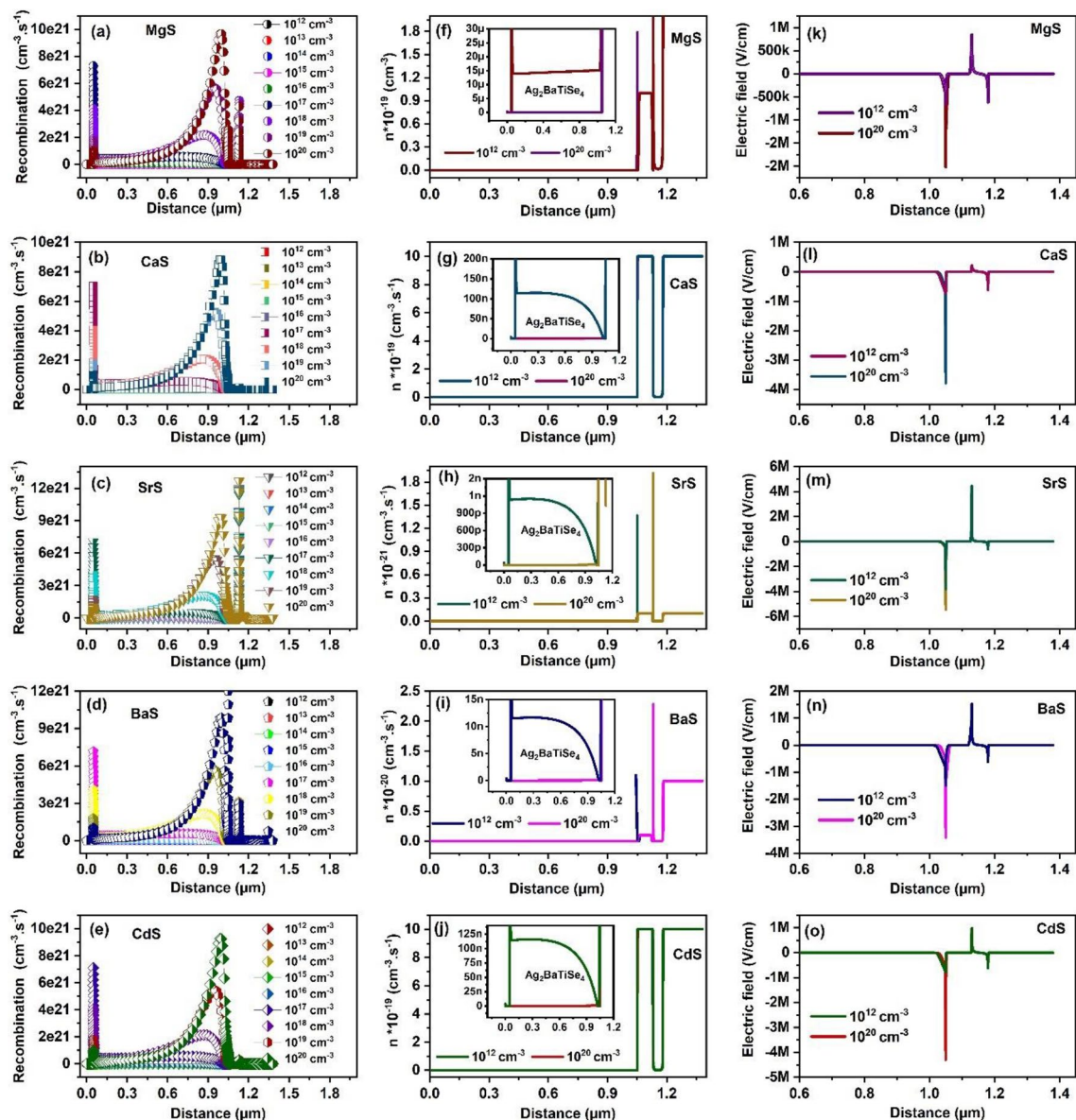
Figure 11. (**a–e**) Recombination rate as a function of defect density of absorber. (**f–j**) Change in the solar cells' density of electrons 'n' with the increasing defect density. The inset displays the variation in 'n' along the absorber region. (**k–o**) Electric field corresponding to defect density of absorber.

cells' overall performance. In light of the obtained results, 10^{15} cm^{-3} is selected as the optimum defect density of Ag$_2$BaTiSe$_4$ for all solar cells.

In addition, it is important to study the influence of absorber's shallow and deep level defects on the performance of solar cells. Hence, we investigated the impact of varying the defect location and density in Ag$_2$BaTiSe$_4$ absorbers on the photovoltaic parameters of solar cells. The observed variation in V$_{OC}$ and J$_{SC}$ are displayed in Fig. 12 while the changes in FF and PCE are provided in Fig. 13. We varied the defect location from − 0.1 to 1.3 eV, corresponding to the valence band and defect density from 10^{12} to 10^{20} cm^{-3}. We found that the photovoltaic parameters were independent of the defect's position up to 10^{15} cm^{-3}, after which they declined with increasing defects. Shallow-level defects, located near/inside the valence and conduction band, were observed in the regions between − 0.1 and 0.1 eV and 1.1 to 1.3 eV, while deep-level defects were present in the region between 0.1 and 1.1 eV due to their presence away from the energy bands[103]. V$_{OC}$ and FF were almost unchanged at shallow levels near the valence band when the defect density was larger than 10^{15} cm^{-3}. However, they slightly decreased when the defects were near the conduction band and drastically fell at the deep levels in all solar cells. Similarly, J$_{SC}$ nearly retained its maximum value at shallow levels when the defect density was increased from 10^{15} to 10^{18} cm^{-3}, while it decreased for deep levels. For defects > 10^{18} cm^{-3}, it showed a decline, even at shallow levels, where the decrement was more pronounced at the deep levels. PCE was largely dependent on J$_{SC}$ rather than V$_{OC}$ and FF. Shallow-level defects aided in the formation of proper band alignment at the interface of transport layers, enriching charge carrier transportation, and had little effect on PCE until 10^{18} cm^{-3}, beyond which they degraded PCE[45]. On the other hand, deep-level defects caused a dramatic reduction in PCE, with the lowest PCEs
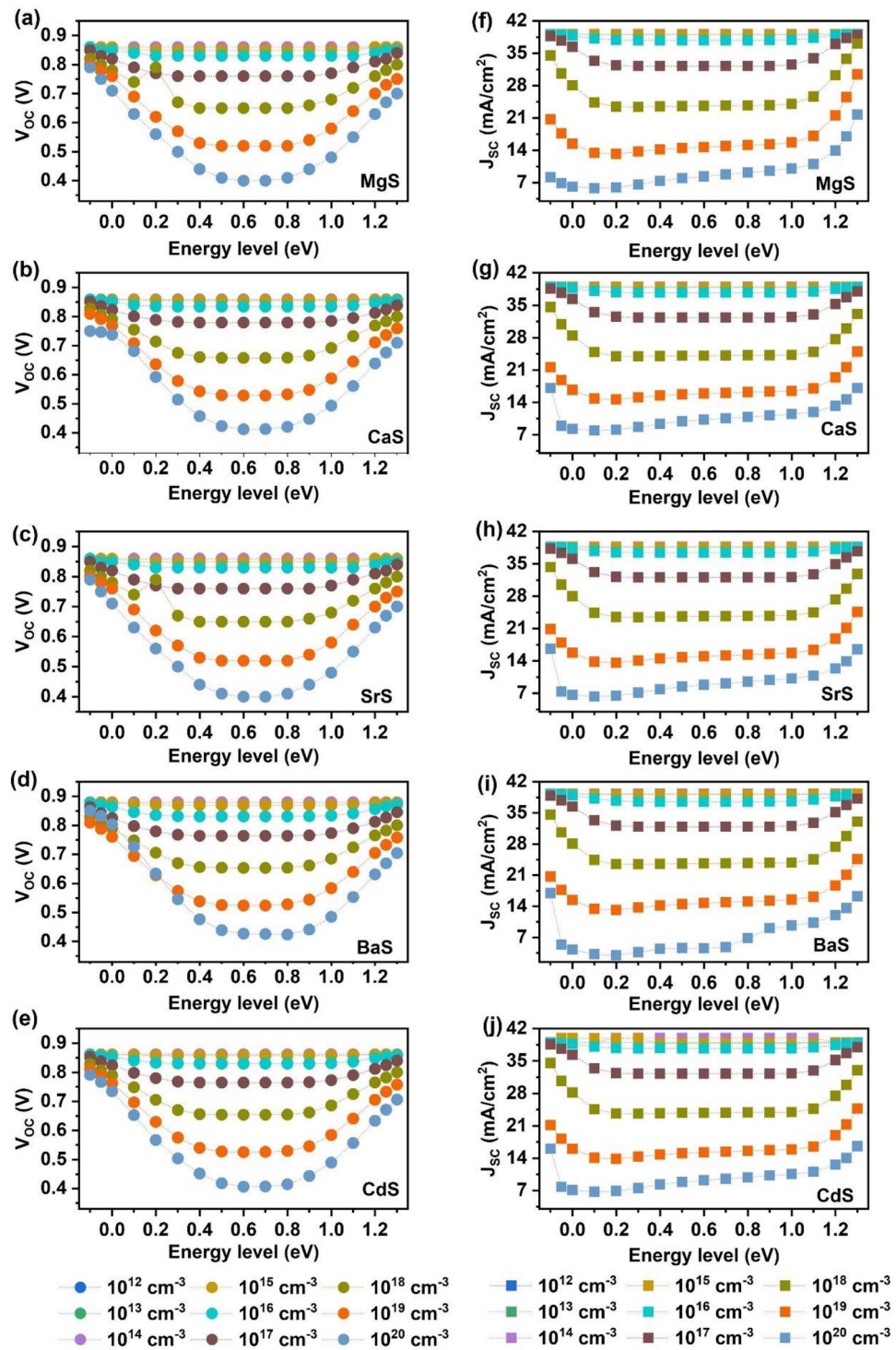
Figure 12. Effect of absorber's defect energy level and density on (**a–e**) V_{OC} and (**f–j**) J_{SC} of novel $Ag_2BaTiSe_4$ solar cells with diverse buffers.

of 1.71%, 2.67%, 2.24%, 0.45%, and 2.35% in MgS, CaS, SrS, BaS, and CdS-based solar cells respectively, obtained at ~0.6 eV for 10^{20} cm^{-3}. This occurs because a large number of photogenerated electrons and holes are trapped due to the presence of deep-level defects in the mid-bandgap regions, leading to high recombination and limiting the separation of charge carriers to the transport layers, degrading the overall performance of solar cells[45,104]. Therefore, to achieve the highest PCE, the deep-level and shallow-level defects in $Ag_2BaTiSe_4$ absorbers must be less than 10^{15} cm^{-3} and 10^{18} cm^{-3}, respectively.
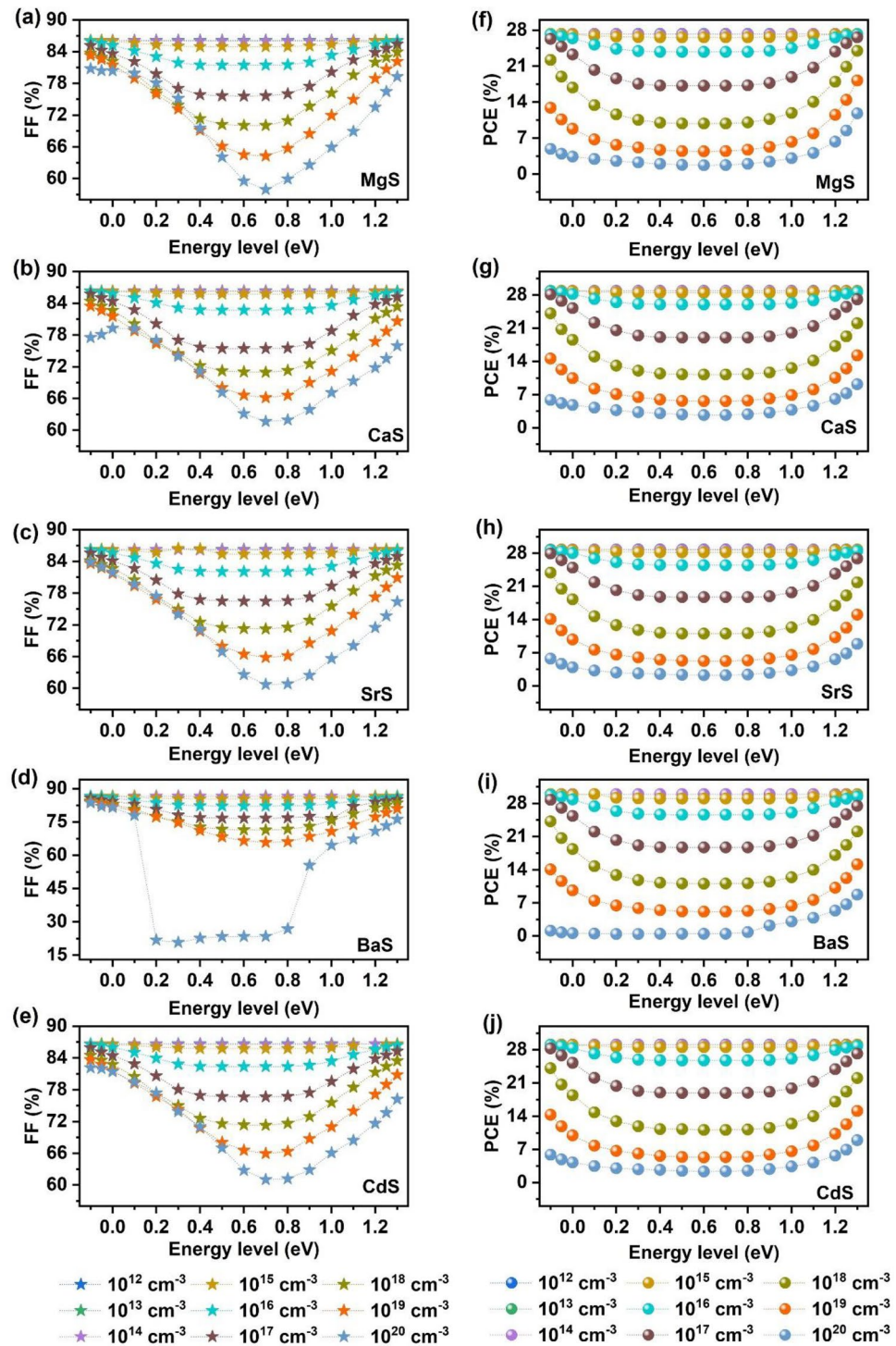
Figure 13. Effect of absorber's defect energy level and density on (**a**–**e**) FF and (**f**–**j**) PCE of novel Ag$_2$BaTiSe$_4$ solar cells with diverse buffers.

Optimization of MoSe$_2$

In I$_2$-II-IV-VI$_4$ thin film solar cells, the formation of MoSe$_2$ is inevitable at the absorber/Mo interface due to the requisite selenization process[105]. MoSe$_2$ belongs to the transition metal dichalcogenide semiconductor family which possess excellent structural, physical and optoelectronic properties owing to its 2D structure[106]. It displays both n and p-type characteristics. In practice, it has been found that p-MoSe$_2$ is helpful for improving solar cell performance as it forms ohmic contact at the junction between the absorber and Mo. Conversely, n-MoSe$_2$ creates a Schottky barrier that enhances back contact recombination[107]. Y. Song et al. have improved the p-type conductivity of MoSe$_2$ by doping Nb and have shown that p-MoSe$_2$ reduces the barrier for hole collection at the

back contact and suppresses interfacial recombination at the absorber/Mo junction[108]. Thus, to understand the role of p-MoSe$_2$ properties on the performance of novel Ag$_2$BaTiSe$_4$ solar cells, its thickness and carrier concentration are varied from 0.050 to 0.2 μm and 10^{12} to 10^{20} cm^{-3} respectively.

Effect of MoSe$_2$'s thickness and carrier concentration

Optimizing the thickness of MoSe$_2$ is critical for improving the performance of solar cells. When the MoSe$_2$ layer is very thin, it increases recombination near the back contact. On the other hand, if the MoSe$_2$ layer is too thick, it reduces the thickness of the Mo layer, degrading the electrical contact of the absorber to Mo and increasing the R$_S$ in the solar cells[105,109]. Thus, in this study, the MoSe$_2$ thickness was varied from 0.050 to 0.2 μm in all solar cells to determine the optimal value (Fig. S5). However, it was found that the variations in the V$_{OC}$, J$_{SC}$, FF, and PCE with respect to MoSe$_2$'s thickness were insignificant. According to literature reports, the thickness of MoSe$_2$ in I$_2$-II-IV-VI$_4$ solar cells is typically in the range of a few 0.1 μm to ~ 1 μm at the interface of absorber/Mo[96,105,109,110]. However, high PCEs were reported for thicknesses in the range of ~ 0.1 to 0.2 μm, indicating that the R$_S$ and back contact recombination could be minimized in this range[7,52]. Therefore, considering the material cost and overall performance, 0.1 μm is considered the optimal value for further simulations. Thereafter, the influence of MoSe$_2$'s carrier concentration on the characteristics of the solar cells is analyzed by differing it from 10^{12} to 10^{20} cm^{-3}. Figure 14 demonstrates the changes in solar cell parameters as a function of MoSe$_2$'s carrier concentration. The corresponding J–V is given in Fig. S6. It can be observed that all solar cells' V$_{OC}$, J$_{SC}$, and PCE almost remain constant till 10^{16} cm^{-3} and then improve to higher values. Conversely, FF drops after 10^{17} cm^{-3} in all solar cells. This observance can be elucidated by the changes in the band alignment corresponding to MoSe$_2$'s carrier concentration (Fig. 15a–e). No change in energy bands is noticed for the concentrations 10^{12}–10^{16} cm^{-3}, referring to the constant solar cell performance till the mentioned range. This also reveals that MoSe$_2$'s carrier concentration must be greater than 10^{16} cm^{-3} to contribute to the solar cell performance significantly. Interestingly, both E$_C$ and E$_V$ of MoSe$_2$ shift upwards for concentrations > 10^{16} cm^{-3}, in consequence of which the barrier for holes is gradually diminished while the electron's barrier is boosted at the Ag$_2$BaTiSe$_4$/MoSe$_2$ interface. This facilitates the transportation of holes from Ag$_2$BaTiSe$_4$ to MoSe$_2$ while restricting the flow of electrons. As a result, the probability of interface recombination declines, which is also witnessed in Fig. 15f–j, where the recombination rate of charge carriers at the Ag$_2$BaTiSe$_4$/MoSe$_2$ interface as a function of MoSe$_2$'s carrier concentration is depicted. The figure shows that as the carrier concentration increases, the recombination rate at the Ag$_2$BaTiSe$_4$/MoSe$_2$ interface drastically falls in all solar cells due to the attainment of appropriate barriers for electrons and holes. This has led to an improvement in V$_{OC}$. In addition, the strong built-in electric field will also be generated at the Ag$_2$BaTiSe$_4$/MoSe$_2$ interface with increasing MoSe$_2$'s carrier concentration, which promotes the collection of holes at the back contact without recombination, causing an enhancement in J$_{SC}$[111,112]. However, the R$_S$ may
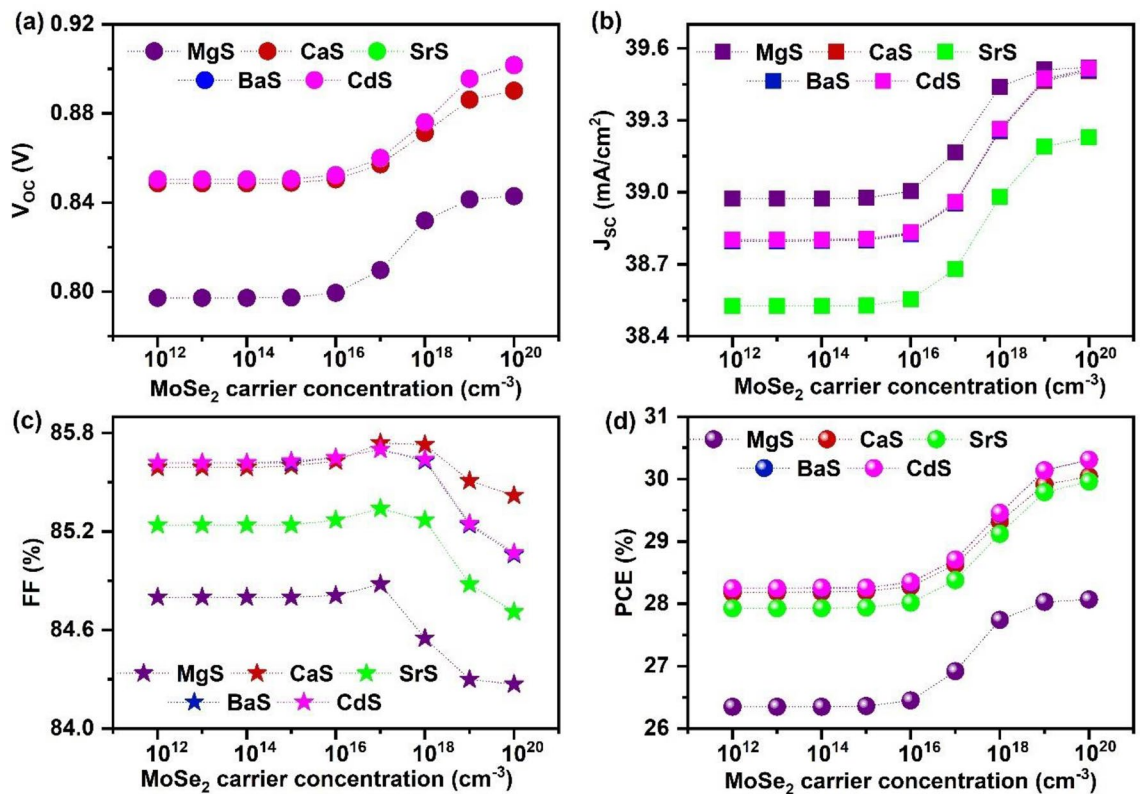

Figure 14. Effect of MoSe$_2$'s carrier concentration on (**a**) V$_{OC}$ (**b**) J$_{SC}$ (**c**) FF (**d**) PCE of novel Ag$_2$BaTiSe$_4$ solar cells with diverse buffers.
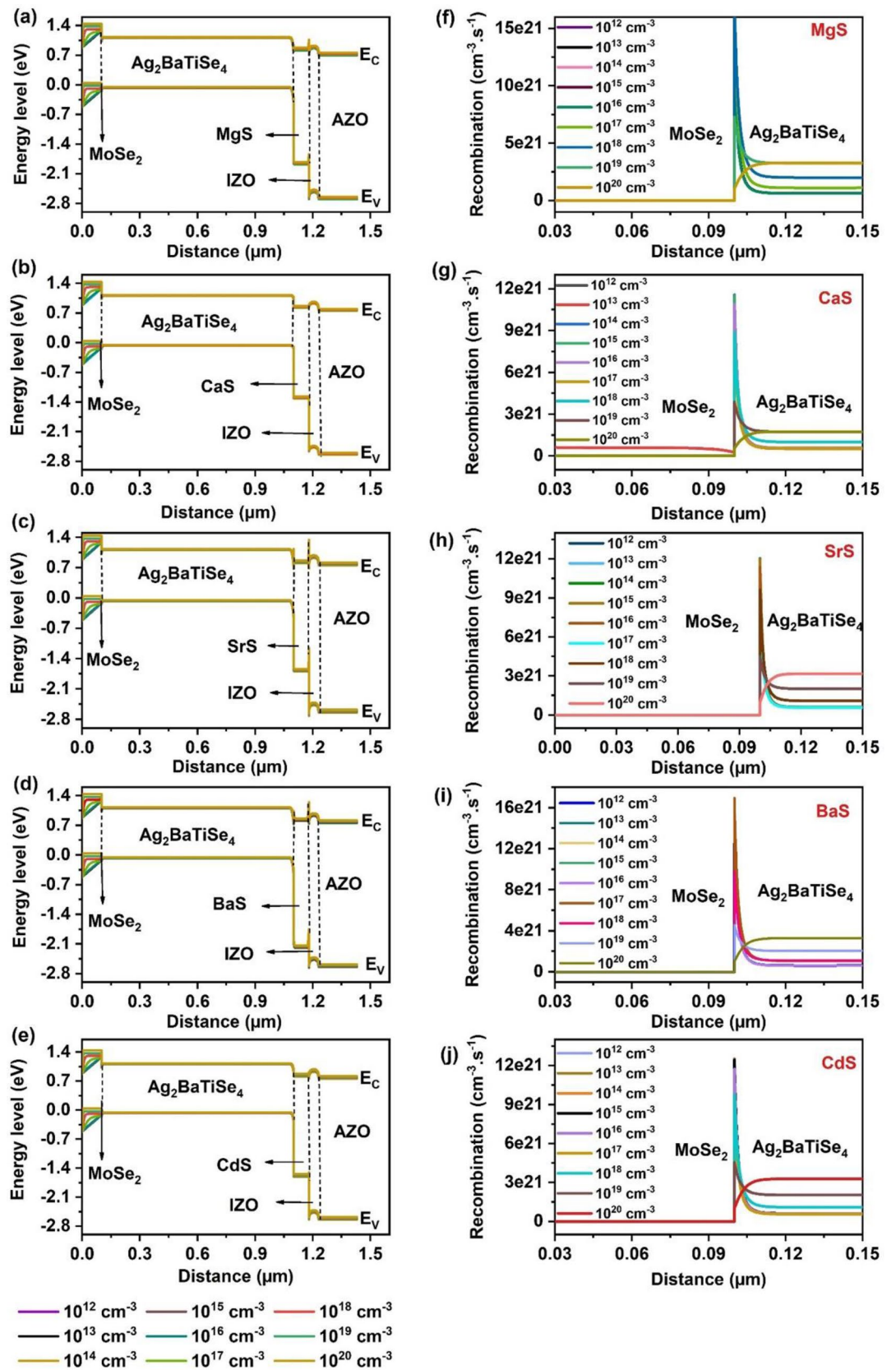
Figure 15. Effect of MoSe$_2$'s carrier concentration on (**a–e**) Energy band alignment and (**f–j**) Recombination rate at Ag$_2$BaTiSe$_4$/MoSe$_2$ interface in novel Ag$_2$BaTiSe$_4$ solar cells with diverse buffers.

increase at higher concentrations, resulting in FF decrement[113]. Nevertheless, the elevation in V_{OC} and J_{SC} has boosted the PCE from 26.35 to 28.07%, 28.18 to 30.04%, 27.93 to 29.96%, 28.25 to 30.31%, and 28.26 to 30.31% in MgS, CaS, SrS, BaS and CdS-based solar cells respectively. Thus, MoSe$_2$'s carrier concentration of 10^{20} cm^{-3} is the optimum value for achieving high PCE in all solar cells.

Effect of defects at Ag$_2$BaTiSe$_4$/buffer and MoSe$_2$/Ag$_2$BaTiSe$_4$ interface

Interface defects are inevitable in solar cells, which are formed during fabrication due to structural imperfections. These defects boost the interface recombination of charge carriers that are detrimental to solar cell performance[67]. Thus, it is crucial to analyze their influence on these solar cells and obtain the optimum value to fabricate them practically. So far, all the simulations were performed with the neutral interface defect density of 10^{12} cm^{-3} at Ag$_2$BaTiSe$_4$/buffer and Ag$_2$BaTiSe$_4$/MoSe$_2$ interface where the defect levels are fixed at 0.6 eV above E_V in all solar cells. Herein, the impact of interface defect density on the photovoltaic parameters is estimated by varying it from 10^{12} to 10^{20} cm^{-3} at both interfaces. The respective variations in J–V characteristics are depicted in Fig. S7. Figure 16a–d demonstrates the outcomes of all solar cells regarding the Ag$_2$BaTiSe$_4$/buffer interface defects. V_{OC} and FF are approximately the same till 10^{15} cm^{-3}, 10^{17} cm^{-3}, 10^{16} cm^{-3}, and 10^{14} cm^{-3} for MgS, SrS, BaS, and CdS-based solar cells, respectively, and decline afterward. In the case of CaS-based solar cells, they drastically reduce beyond 10^{12} cm^{-3}. In contrast, J_{SC} remains stable till 10^{18} cm^{-3} in all solar cells and then decreases. However, the reduction in J_{SC} is less significant compared to V_{OC} and FF. Moreover, the PCE of all solar cells follows a similar trend as V_{OC} and FF, indicating that the overall performance of all solar cells is determined mainly by the changes in V_{OC} and FF while less influenced by J_{SC} at Ag$_2$BaTiSe$_4$/buffer interface. The level of degradation in PCE is observed to be 8.48%, 18.03%, 4.55%, 6.22%, and 13.86% in MgS, CaS, SrS, BaS, and CdS-based solar cells, respectively, for the defect density range 10^{12}–10^{20} cm^{-3}. This clearly reveals that CaS and CdS-based solar cells are more sensitive to the Ag$_2$BaTiSe$_4$/buffer interface defects than the other solar cells. In contrast, SrS-based solar cell is comparatively stable with the defects. The overall degradation in solar cell performance with the interface defects occurs due to the increasing trap-assisted recombination of photogenerated electrons at the buffer/Ag$_2$BaTiSe$_4$ interface, which restricts their flow towards the front contact[114]. Thus, the optimum defect density of 10^{15} cm^{-3}, 10^{12} cm^{-3}, 10^{17} cm^{-3}, 10^{16} cm^{-3}, and 10^{14} cm^{-3} are selected for MgS, CaS, SrS, BaS, and CdS-based solar cells, respectively at Ag$_2$BaTiSe$_4$/buffer interface to attain maximum solar cell performance. These values are higher than the defect densities reported in the experiments at the CZTS/buffer interface, revealing the superiority of novel Ag$_2$BaTiSe$_4$ solar cells over their predecessors[115,116]. Similarly, the defect density at the Ag$_2$BaTiSe$_4$/MoSe$_2$ interface is shifted from 10^{12} to 10^{20} cm^{-3} (Fig. 16e–h). Here, all the solar cell parameters start to reduce for defect density above 10^{15} cm^{-3} and begin to saturate at 10^{18} cm^{-3}. It can be noticed that J_{SC} is adversely affected than V_{OC} and FF, i.e., it decreases from ~ 39 to ~ 34 mA cm^{-2} when defect density is raised from 10^{12} to 10^{18} cm^{-3}. This has led to a decline in PCE by ~ 6.5% in all solar cells. The drop in the solar cell performance may happen because holes travelling from Ag$_2$BaTiSe$_4$ to MoSe$_2$ have a high chance of being trapped or recombined when the defects at the Ag$_2$BaTiSe$_4$/MoSe$_2$ interface increases[114]. The results show that defect density < 10^{15} cm^{-3} is required at the Ag$_2$BaTiSe$_4$/MoSe$_2$ interface for exceptional solar cell performance. Overall, the investigation of interface defects suggests that it has a massive impact on solar cell performance. These defects are generally produced due to the structural defects between different layers and metal cation diffusion through the absorber during fabrication[67]. Thus, effective techniques must be employed for the deposition of layers, and methods such as etching, post-heat treatment, and inserting a passivation layer can be used to minimize the interface defects in solar cells[117–119].

Table 5 displays the final solar cell performance of the novel Ag$_2$BaTiSe$_4$ solar cells with diverse buffers after optimization, and the corresponding J-V is displayed in Fig. 17. As discussed in the introduction, the main problem that limits the PCE of I$_2$-II-IV-VI$_4$ solar cells is their large V_{OC} deficit. In addition, CdS is used as a buffer in most solar cells containing the toxic element Cd, creating severe problems when dumped into the environment. Therefore, developing efficient absorbers and eco-friendly buffers is always highly interesting to the photovoltaic community. In this regard, for the first time, we have reported Ag$_2$BaTiSe$_4$ of group I$_2$-II-IV-VI$_4$ as a potential absorber and a new class of alkaline earth metal chalcogenides, namely MgS, CaS, SrS, and BaS as alternative buffers using SCAPS-1D. Herein, we have accomplished high PCEs of 28.00%, 30.02%, 29.87%, 30.23%, and 29.68% for MgS, CaS, SrS, BaS, and CdS-based Ag$_2$BaTiSe$_4$ solar cells, respectively. Surprisingly, the PCEs achieved in Ag$_2$BaTiSe$_4$ solar cells with alkaline earth metal chalcogenides buffers are comparable with CdS, proving their potential and suitability to be applied as alternative, non-toxic buffers in thin-film solar cells. Moreover, the V_{OC} loss in these solar cells is less, specifically 0.3 V, 0.29 V, 0.34 V, 0.28 V, and 0.29 V for MgS, CaS, SrS, BaS, and CdS-based Ag$_2$BaTiSe$_4$ solar cells respectively, displaying the superior properties of Ag$_2$BaTiSe$_4$ as an alternative absorber. The low V_{OC} deficit in alkaline earth metal chalcogenides buffer-based Ag$_2$BaTiSe$_4$ solar cells is highly possible in experiments due to the proper band alignment at absorber/buffer interface and low antisite defects in Ag$_2$BaTiSe$_4$ absorber because of the large atomic size difference between the constituent elements. Thus, this work would kindle the photovoltaic community's interest in fabricating novel efficient Ag$_2$BaTiSe$_4$ solar cells with new alkaline earth metal chalcogenides buffers and achieve high PCE. In addition, based on our research outcomes, we propose that these new alkaline earth metal chalcogenides buffers have immense potential to be utilized in other conventional solar cells such as CdTe, CIGSSe, perovskites, etc.

Overall, after the optimization of buffer, Ag$_2$BaTiSe$_4$, MoSe$_2$, and interface properties, the PCE incredibly improved from 18.72%, 11.65%, 15.93%, 15.47% and 14.99% to 28.00%, 30.02%, 29.87%, 30.23% and 29.68% for MgS, CaS, SrS, BaS and CdS-based Ag$_2$BaTiSe$_4$ solar cells respectively. Further, the final solar cells where the high PCEs have been demonstrated are selected for the upcoming studies to investigate the impact of R_S, R_{Sh}, and working temperature on their performance.
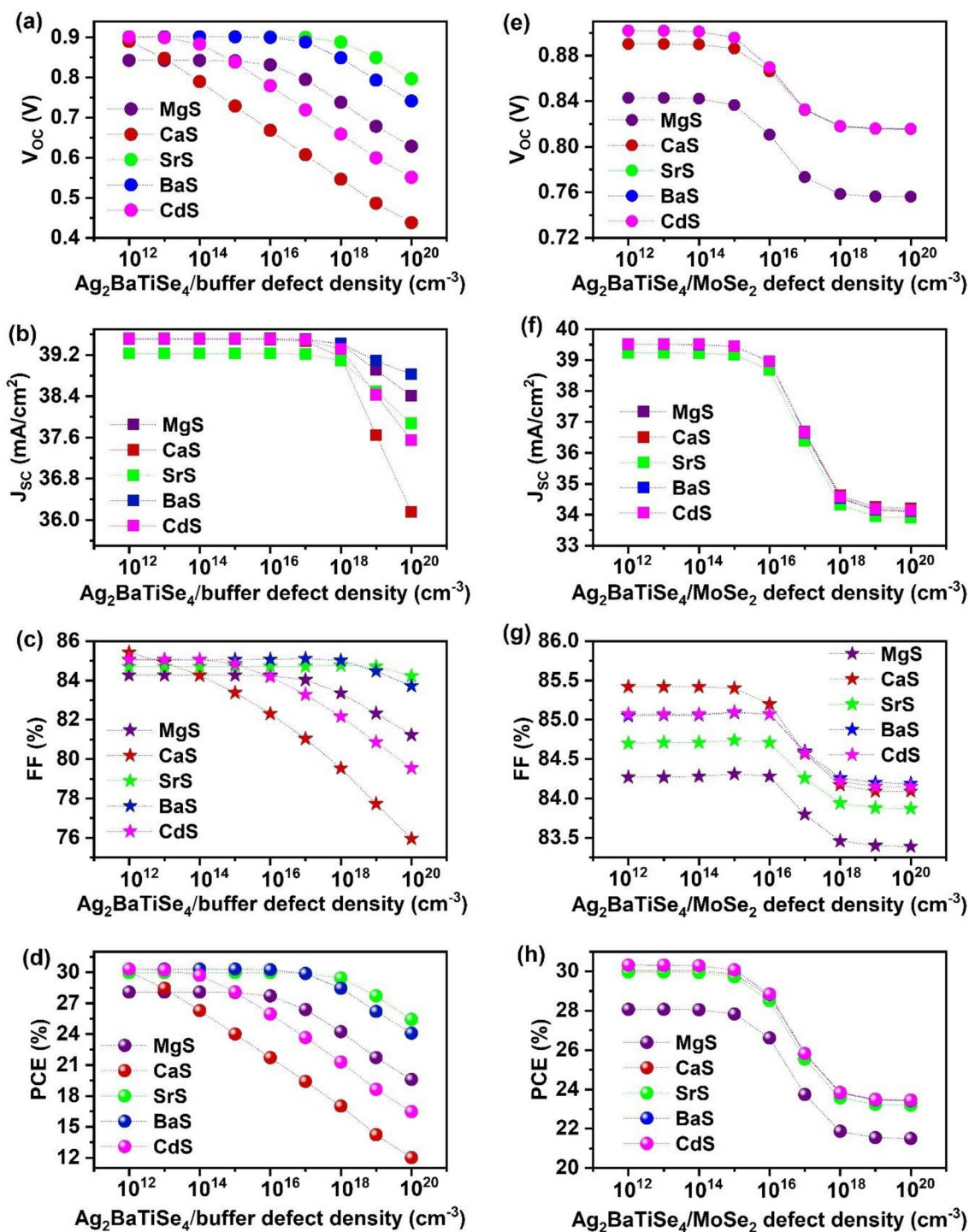
Figure 16. Effect of defect density at Ag$_2$BaTiSe$_4$/buffer and Ag$_2$BaTiSe$_4$/MoSe$_2$ interface on the photovoltaic parameters of novel Ag$_2$BaTiSe$_4$ solar cells with diverse buffers.

Solar cell structure	V$_{OC}$ (V)	J$_{SC}$ (mA cm^{-2})	FF (%)	PCE (%)
AZO/IZO/MgS/Ag$_2$BaTiSe$_4$/MoSe$_2$/Mo	0.840	39.51	84.28	28.00
AZO/IZO/CaS/Ag$_2$BaTiSe$_4$/MoSe$_2$/Mo	0.889	39.49	85.42	30.02
AZO/IZO/SrS/Ag$_2$BaTiSe$_4$/MoSe$_2$/Mo	0.899	39.20	84.72	29.87
AZO/IZO/BaS/Ag$_2$BaTiSe$_4$/MoSe$_2$/Mo	0.899	39.50	85.07	30.23
AZO/IZO/CdS/Ag$_2$BaTiSe$_4$/MoSe$_2$/Mo	0.883	39.50	85.06	29.68

Table 5. Solar cell parameters of novel Ag$_2$BaTiSe$_4$ solar cells with diverse buffers after optimization.
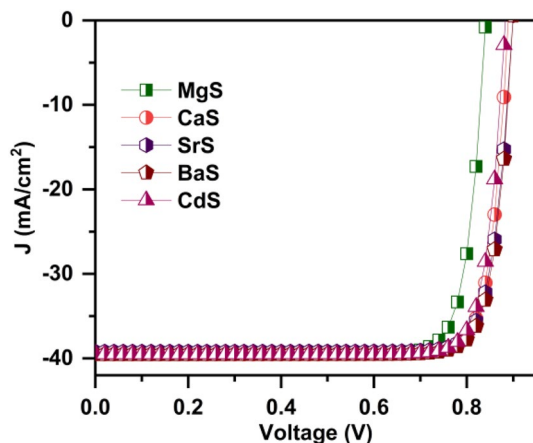
Figure 17. J–V graph of novel $Ag_2BaTiSe_4$ solar cells with diverse buffers after optimization.

Effect of series and shunt resistances

R_S and R_{Sh} display significant impact on the performance of solar cells. R_S is the sum of resistance at the front and back contacts and between various layers of solar cells. On the other hand, R_{Sh} originates from the reverse saturation current in solar cells that is produced by the manufacturing defects[120]. Here, the influence of R_S and R_{Sh} on the solar cell parameters is investigated using SCAPS-1D. Figure 18a–d displays V_{OC}, J_{SC}, FF, and PCE as a function of R_S, where it is varied from 0.5 to 6 Ω cm^2 for all solar cells. The respective variations in J–V characteristics are depicted in Fig. S8. It can be observed that V_{OC} and J_{SC} remain unaffected throughout the R_S range. Whereas, FF drastically decreases from 82.12 to 59.27%, 83.34 to 61.27%, 82.72 to 61.35%, 83.05 to 61.49%, and 82.99 to 60.96% in MgS, CaS, SrS, BaS and CdS-based solar cells respectively. The massive reduction in FF is attributed to the colossal power loss in the solar cells with increasing R_S, which adversely affects their performance[121]. Thus, when R_S is improved from 0.5 to 6 Ω cm^2, PCE dramatically declined by ~7.5% in all the solar cells. Similarly, R_{Sh} is tuned from 1000 to 100,000 Ω cm^2 in all solar cells, as shown in Fig. 18e–h. The respective changes in J–V are depicted in Fig. S8. In this case, V_{OC} and J_{SC} are almost the same for all R_{Sh} values. On the contrary, the FF and PCE values enhanced with an increment in the R_{Sh} till 2000 Ω cm^2 and saturate on further increase in R_{Sh}. Nevertheless, the rise in PCE is about 0.53%, 0.61%, 0.62%, 0.7%, and 0.6% in MgS, CaS, SrS, BaS, and CdS-based solar cells, respectively. This exhibits that the effect of R_{Sh} on the performance of these solar cells is negligible compared to R_S. Therefore, a low R_S of 0.5 Ω cm^2 is highly recommended for the efficient functioning of these novel $Ag_2BaTiSe_4$ solar cells.

Effect of working temperature

Long-term stability in the environment is an essential requirement for the application of solar cells[122]. Thus, the deterioration process of solar cells under ambient air conditions must be investigated. In the present study, the working temperature is varied from 300 to 400 K for analyzing its influence on all solar cells. Figure 18i–l demonstrates the response of solar cells concerning working temperature. The corresponding variations in J–V graphs are depicted in Fig. S8. It can be seen that V_{OC}, FF, and PCE diminish with increasing temperature while J_{SC} slightly increases in all solar cells. The temperature rise reduces the bandgap of the absorber, which enhances the charge carrier generation in solar cells, leading to enhancement in J_{SC}[122]. However, the thermally generated electrons begin to vibrate at high temperatures, become unstable, and recombine with the holes before being collected at the contacts, reducing V_{OC}. Moreover, the increasing temperature affects the transport efficiency of charge carriers, such as carrier concentration and mobility of charge carriers, thereby decreasing the FF of all solar cells[123]. Overall, the combined decrement in V_{OC} and FF has led to a lowering of PCE from 28.0% to 21.64%, 30.02 to 24.46%, 29.87 to 24.23%, 30.23 to 24.39%, 29.68 to 24.17% for MgS, CaS, SrS, BaS, and CdS-based solar cells respectively.

Conclusion

In the present work, a comprehensive numerical study on the performance of novel $Ag_2BaTiSe_4$ solar cells with new alkaline earth metal chalcogenides as alternative buffers to CdS was performed using SCAPS-1D. Upon optimizing buffer properties, maximum PCE of 18.84%, 17.17%, 20.65%, 20.87%, and 18.66% for MgS, CaS, SrS, BaS, and CdS-based respective solar cells were obtained, which mainly originated from the variation in $N_{D\,buffer}$. The energy bands shifted downwards for $N_{D\,buffer} > N_{A\,absorber}$, diminishing the barrier height at the absorber/buffer interface, eventually suppressing the recombination rate and enhancing the V_b and W of solar cells. Thereafter, at the optimized absorber's electron affinity (4.4 eV) and thickness (1 μm), PCE improved by 5.33% for CaS-based solar cells and ~2% for other solar cells due to the increment in R_{rec} and light absorption of solar cells, as evidenced by Nyquist plots and QE measurements. Notably, the absorber's carrier concentration of 10^{18} cm^{-3} drastically escalated the performance of all solar cells, while its defect density > 10^{15} cm^{-3} declined the PCE owing to the dramatic decrease in the τ and L of charge carriers. Further, on tuning MoSe$_2$ parameters and interfacial properties, the best PCE of 28%, 30.02%, 29.87%, 30.23%, and 29.68% was achieved with minimal V_{OC} loss
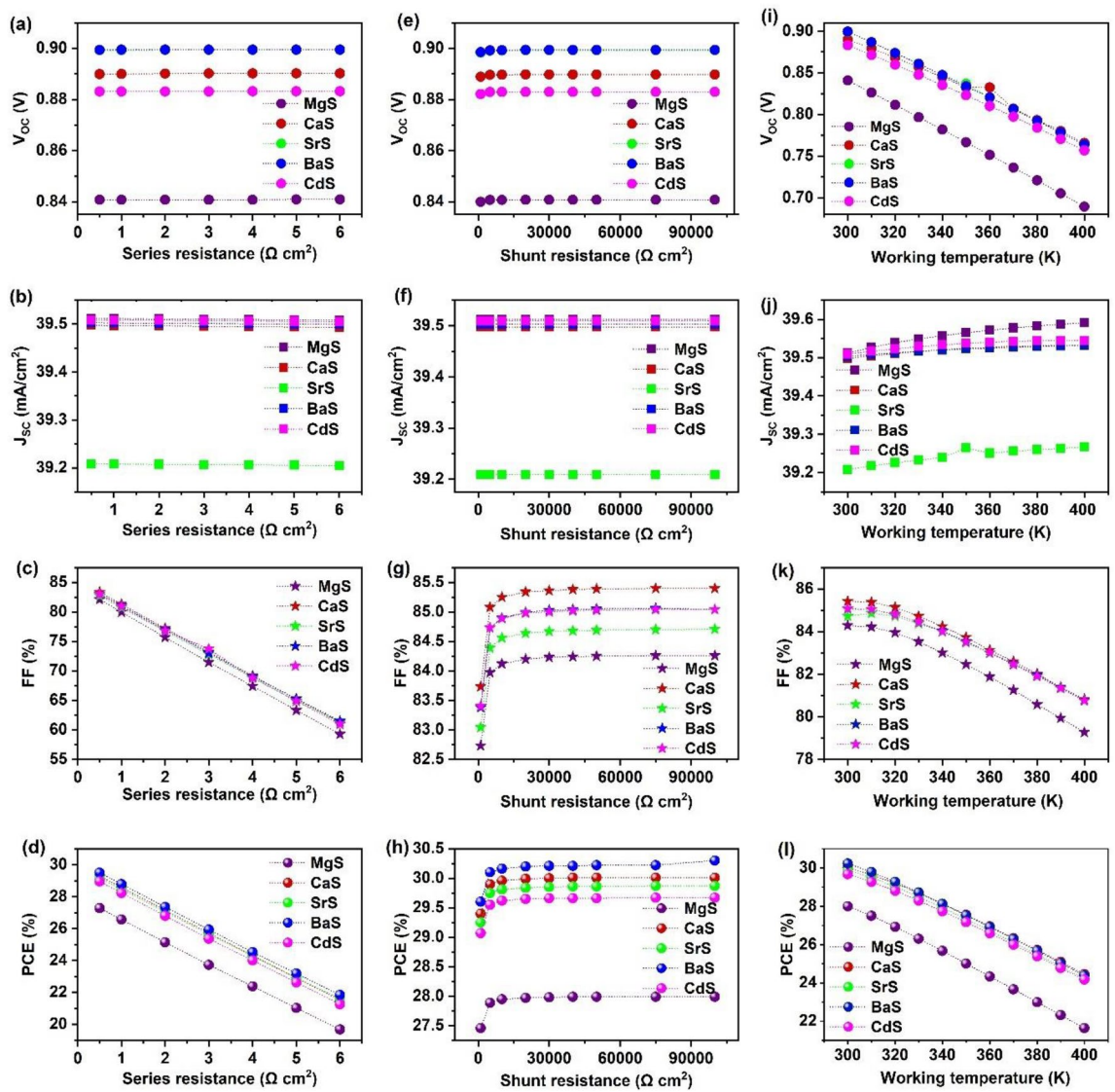
Figure 18. Effect of series resistance, shunt resistance, and working temperature on the performance of novel Ag$_2$BaTiSe$_4$ solar cells with diverse buffers.

of ~ 0.3 V for MgS, CaS, SrS, BaS, and CdS-based solar cells respectively. Therefore, this work could open constructive research avenues for the photovoltaic community to fabricate highly efficient thin-film solar cells using novel Ag$_2$BaTiSe$_4$ as an absorber and new alkaline earth metal chalcogenides as alternative, non-toxic buffers.

Data availability
The data that support the findings of this study are provided in the supplementary material of this article, and further required data are available from the corresponding author upon reasonable request.

References
1. Mehmood, B., Khan, M. I., Iqbal, M., Mahmood, A. & Al-Masry, W. Structural and optical properties of Ti and Cu co-doped ZnO thin films for photovoltaic applications of dye sensitized solar cells. *Int. J. Energy Res.* **45**, 2445–2459 (2021).
2. Stern, P. C. *et al.* Opportunities and insights for reducing fossil fuel consumption by households and organizations. *Nat. Energy* **1**, 16043 (2016).
3. Whitesides, G. M. & Crabtree, G. W. Don't forget long-term fundamental research in energy. *Science* **1979**(315), 796–798 (2007).
4. Green, M. A., Ho-Baillie, A. & Snaith, H. J. The emergence of perovskite solar cells. *Nat. Photon.* **8**, 506–514 (2014).
5. Nakamura, M. *et al.* Cd-Free Cu(In, Ga)(Se, S)2 thin-film solar cell with record efficiency of 23.35%. *IEEE J. Photovolt.* **9**, 1863–1867 (2019).
6. Green, M. *et al.* Solar cell efficiency tables (version 57). *Prog. Photovolt. Res. Appl.* **29**, 3–15 (2021).
7. Wang, W. *et al.* Device characteristics of CZTSSe thin-film solar cells with 12.6% efficiency. *Adv. Energy Mater.* **4**, 1301465 (2014).

8. Zhou, J. *et al.* Control of the phase evolution of kesterite by tuning of the selenium partial pressure for solar cells with 13.8% certified efficiency. *Nat. Energy* **8**, 526–535 (2023).

9. Nisika, K. K. & Kumar, M. Progress and prospects of CZTSSe/CdS interface engineering to combat high open-circuit voltage deficit of kesterite photovoltaics: A critical review. *J. Mater. Chem. A Mater.* **8**, 21547–21584 (2020).

10. Green, M. A. *et al.* Solar cell efficiency tables (version 62). *Prog. Photovolt. Res. Appl.* **31**, 651–663 (2023).

11. Mitzi, D. B., Gunawan, O., Todorov, T. K. & Barkhouse, D. A. R. Prospects and performance limitations for Cu–Zn–Sn–S–Se photovoltaic technology. *Philos. Trans. R. Soc. A Math. Phys. Eng. Sci.* **371**, 20110432 (2013).

12. Chen, S., Walsh, A., Gong, X.-G. & Wei, S.-H. Classification of lattice defects in the kesterite Cu$_2$ZnSnS$_4$ and Cu$_2$ZnSnSe$_4$ earth-abundant solar cell absorbers. *Adv. Mater.* **25**, 1522–1539 (2013).

13. Fan, P. *et al.* Over 10% efficient Cu$_2$CdSnS$_4$ solar cells fabricated from optimized sulfurization. *Adv. Funct. Mater.* **32**, 2207470 (2022).

14. Chatterjee, S. & Pal, A. J. A solution approach to p-type Cu$_2$FeSnS$_4$ thin-films and pn-junction solar cells: Role of electron selective materials on their performance. *Sol. Energy Mater Sol. Cells* **160**, 233–240 (2017).

15. Shin, D. *et al.* Earth-abundant chalcogenide photovoltaic devices with over 5% efficiency based on a Cu$_2$BaSn(S, Se)4 absorber. *Adv. Mat.* **29**, 1606945 (2017).

16. Crovetto, A. *et al.* Wide band gap Cu$_2$SrSnS$_4$ solar cells from oxide precursors. *ACS Appl. Energy Mater.* **2**, 7340–7344 (2019).

17. Elsaeedy, H. I. Growth, structure, optical and optoelectrical characterizations of the Cu$_2$NiSnS$_4$ thin films synthesized by spray pyrolysis technique. *J. Mater. Sci. Mater. Electron.* **30**, 12545–12554 (2019).

18. El Radaf, I. M., Elsaeedy, H. I., Yakout, H. A. & El Sayed, M. T. Junction parameters and electrical characterization of the Al/n-Si/Cu$_2$CoSnS$_4$/Au heterojunction. *J. Electron. Mater.* **48**, 6480–6486 (2019).

19. Prabhakar, R. R. *et al.* Photovoltaic effect in earth abundant solution processed Cu$_2$MnSnS$_4$ and Cu$_2$MnSn(S, Se)4 thin films. *Sol. Energy Mater Sol. Cells* **157**, 867–873 (2016).

20. Ma, C. *et al.* The preparation of Ag$_2$ZnSnS$_4$ homojunction solar cells. *Mater. Lett.* **207**, 209–212 (2017).

21. Gershon, T. *et al.* Photovoltaic device with over 5% efficiency based on an n-Type Ag$_2$ZnSnSe$_4$ absorber. *Adv. Energy Mater.* **6**, 1601182 (2016).

22. Yee, Y. S., Magyari-Köpe, B., Nishi, Y., Bent, S. F. & Clemens, B. M. Deep recombination centers in Cu$_2$ZnSnSe$_4$ revealed by screened-exchange hybrid density functional theory. *Phys. Rev. B* **92**, 195201 (2015).

23. Wang, Z., Cai, J., Wang, Q., Wu, S. & Li, J. Unsupervised discovery of thin-film photovoltaic materials from unlabeled data. *NPJ Comput. Mater.* **7**, 128 (2021).

24. Zyoud, S. H., Zyoud, A. H., Ahmed, N. M. & Abdelkader, A. F. I. Numerical modelling analysis for carrier concentration level optimization of CdTe heterojunction thin film-based solar cell with different non-toxic metal chalcogenide buffer layers replacements: Using SCAPS–1D software. *Crystals Basel* **11**, 1454 (2021).

25. Kim, J. *et al.* Optimization of sputtered ZnS buffer for Cu$_2$ZnSnS$_4$ thin film solar cells. *Thin Solid Films* **566**, 88–92 (2014).

26. Barkhouse, D. A. R. *et al.* Cd-free buffer layer materials on Cu$_2$ZnSn(S$_x$Se$_{1−x}$)$_4$: Band alignments with ZnO, ZnS, and In2S3. *Appl. Phys. Lett.* **100**, 125 (2012).

27. Li, J. *et al.* Restraining the band fluctuation of CBD-Zn(O, S) layer: Modifying the hetero-junction interface for high performance C$_u$2ZnSnS$_e$4 solar cells with Cd-free buffer layer. *Sol. RRL* **1**, 1700075 (2017).

28. Rajeshmon, V. G., Poornima, N., Sudha-Kartha, C. & Vijayakumar, K. P. Modification of the optoelectronic properties of sprayed In2S3 thin films by indium diffusion for application as buffer layer in CZTS based solar cell. *J. Alloys Compd.* **553**, 239–244 (2013).

29. Alam, M. J. *et al.* Improving optical properties and controlling defect-bound states in ZnMgO thin films through ultraviolet–ozone annealing. *Thin Solid Films* **708**, 138112 (2020).

30. Ameri, M. *et al.* FP-LMTO calculations of structural and electronic properties of alkaline-earth chalcogenides alloys AY: A = Ca, Sr, Ba; Y = S. *Mater. Sci. Appl.* **3**, 861–871 (2012).

31. Yisau, B., Babatunde, R. A. & Bolanle, Y. I. Effect of annealing on optical and electrical properties of magnesium sulphide (MgS) thin film grown by chemical bath deposition method. *Int. J. Sci. Res. Phys. Appl. Sci.* **8**, 60–64 (2020).

32. Taleatu, B. A. *et al.* Microstructural and optical properties of nanocrystalline MgS thin film as wide band gap barrier material. *Appl. Phys. A* **118**, 539–545 (2015).

33. Siraj, H., Ahmad, K. S., Jaffri, S. B. & Sohail, M. Synthesis, characterization and electrochemical investigation of physical vapor deposited barium sulphide doped iron sulphide dithiocarbamate thin films. *Microelectron. Eng.* **233**, 111400 (2020).

34. Ijeoma, N. Effect of film thickness on the transmittance of chemical bath deposited barium sulphide (BaS) thin film. *Int. J. Innov. Res. Adv. Stud.* **4**, 365–367 (2017).

35. Samuel, S. O. *et al.* Influence of deposition voltage on strontium sulphide doped silver for optoelectronic application. *East Eur. J. Phys.* **2023**, 189–196 (2023).

36. Nowsherwan, G. A. *et al.* Numerical optimization and performance evaluation of ZnPC:PC70BM based dye-sensitized solar cell. *Sci. Rep.* **13**, 10431 (2023).

37. Montoya De Los Santos, I. *et al.* Optimization of CH$_3$NH$_3$PbI$_3$ perovskite solar cells: A theoretical and experimental study. *Sol. Energy* **199**, 198–205 (2020).

38. Houimi, A., Gezgin, S. Y., Mercimek, B. & Kılıç, H. Ş. Numerical analysis of CZTS/n-Si solar cells using SCAPS-1D. A comparative study between experimental and calculated outputs. *Opt. Mater. Amst.* **121**, 111544 (2021).

39. Ashok, A., Valencia, D., Conde, J. & Velumani, S. Simulation of theoretical and experimental parameters of materials used in CIGSe thin film solar cells by SCAPS software. In *2022 19th International Conference on Electrical Engineering, Computing Science and Automatic Control (CCE)* 1–6 (IEEE, 2022).

40. Karade, V. C. *et al.* Combating open circuit voltage loss in Sb$_2$Se$_3$ solar cell with an application of SnS as a back surface field layer. *Sol. Energy* **233**, 435–445 (2022).

41. Burgelman, M., Nollet, P. & Degrave, S. Modelling polycrystalline semiconductor solar cells. *Thin Solid Films* **361–362**, 527–532 (2000).

42. Nykyruy, L. I., Yavorskyi, R. S., Zapukhlyak, Z. R., Wisz, G. & Potera, P. Evaluation of CdS/CdTe thin film solar cells: SCAPS thickness simulation and analysis of optical properties. *Opt. Mater. (Amst.)* **92**, 319–329 (2019).

43. Ashraf, M. A. & Alam, I. Numerical simulation of CIGS, CISSe and CZTS-based solar cells with In$_2$S$_3$ as buffer layer and Au as back contact using SCAPS 1D. *Eng. Res. Express.* **2**, 035015 (2020).

44. Bansal, N. K., Porwal, S., Dixit, H., Kumar, D. & Singh, T. A theoretical study to investigate the impact of bilayer interfacial modification in perovskite solar cell. *Energy Technol.* **11**, 4 (2023).

45. Arockiya-Dass, K. T., Sekar, K. & Marasamy, L. Theoretical insights of degenerate ZrS2 as a new buffer for highly efficient emerging thin-film solar cells. *Energy Technol.* **11**, 9 (2023).

46. Kukreti, S., Gupta, G. K. & Dixit, A. Theoretical DFT studies of Cu$_2$HgSnS$_4$ absorber material and Al:ZnO/ZnO/CdS/Cu$_2$HgSnS$_4$/Back contact heterojunction solar cell. *Sol. Energy* **225**, 802–813 (2021).

47. Ghebouli, M. A., Choutri, H. & Bouarissa, N. Band structure, structural properties and stability of Ca$_x$ Mg$_{1−x}$ S alloys. *Phys. Scr.* **87**, 015701 (2013).

48. Farrell, S. P. *et al.* Evolution of local electronic structure in alabandite and niningerite solid solutions [(Mn, Fe)S, (Mg, Mn)S, (Mg, Fe)S] using sulfur K - and L -edge XANES spectroscopy. *Am. Mineral.* **87**, 1321–1332 (2002).

49. Lin, H.-F., Lau, W.-M. & Zhao, J. Magnetism in the p-type monolayer II-VI semiconductors SrS and SrSe. *Sci. Rep.* **7**, 45869 (2017).
50. Absike, H., Labrim, H., Hartiti, B. & Ez-Zahraouy, H. Effects of Si doping on the structural, electronic and optical properties of barium chalcogenide BaS: A first-principles study. *SPIN* **10**, 2 (2020).
51. Akcay, N., Zaretskaya, E. P. & Ozcelik, S. Development of a CZTS solar cell with CdS buffer layer deposited by RF magnetron sputtering. *J. Alloys Compd.* **772**, 782–792 (2019).
52. Li, J. *et al.* Defect control for 12.5% efficiency Cu2ZnSnSe4 kesterite thin-film solar cells by engineering of local chemical environment. *Adv. Mater.* **32**, 2005268 (2020).
53. Park, J. Y., Chalapathy, R. B. V., Lokhande, A. C., Hong, C. W. & Kim, J. H. Fabrication of earth abundant $Cu_2ZnSn(S, Se)4$ (CZTSSe) thin film solar cells with cadmium free zinc sulfide (ZnS) buffer layers. *J. Alloys Compd.* **695**, 2652–2660 (2017).
54. Choubrac, L. *et al.* 76% CZGSe solar cells thanks to optimized CdS chemical bath deposition. *Phys. Status Solidi A* **215**, 13 (2018).
55. Shin, B. *et al.* Thin film solar cell with 8.4% power conversion efficiency using an earth-abundant Cu2ZnSnS4 absorber. *Prog. Photovolt: Res. Appl* **21**, 72–76 (2013).
56. ElAnzeery, H. *et al.* Refractive index extraction and thickness optimization of $Cu_2ZnSnSe_4$ thin film solar cells. *Phys. Status Solidi (a)* **212**, 1984–1990 (2015).
57. Lu, Y., Wang, S., Yang, M., Xu, X. & Li, Q. Comparative study of AZO and ITO thin film sputtered at different temperatures and their application in Cu_2ZnSnS_4 solar cells. *J. Mater. Sci. Mater. Electron.* **29**, 17525–17532 (2018).
58. Chen, Z. *et al.* Solution-processed trigonal Cu_2BaSnS_4 thin-film solar cells. *ACS Appl. Energy Mater.* **1**, 3420–3427 (2018).
59. Ishizuka, S. *et al.* Fabrication of wide-gap $Cu(In_{1-x}Ga_x)Se_2$ thin film solar cells: A study on the correlation of cell performance with highly resistive i-ZnO layer thickness. *Sol. Energy Mater. Sol. Cells* **87**, 541–548 (2005).
60. Jahagirdar, A., Kadam, A. & Dhere, N. Role of i-ZnO in optimizing open circuit voltage of $CIGS_2$ and CIGS thin film solar cells. In *2006 IEEE 4th World Conference on Photovoltaic Energy Conference* 557–559 (IEEE, 2006).
61. Regmi, G. & Velumani, S. Impact of target power on the properties of sputtered intrinsic zinc oxide (i-ZnO) thin films and its thickness dependence performance on CISe solar cells. *Opt. Mater. Amst.* **119**, 111350 (2021).
62. Marasamy, L. *et al.* Probing the significance of RF magnetron sputtering conditions on the physical properties of CdS thin films for ultra-thin CdTe photovoltaic applications. *Appl. Surf. Sci.* **574**, 151640 (2022).
63. Shah, D. K. *et al.* A simulation approach for investigating the performances of cadmium telluride solar cells using doping concentrations, carrier lifetimes, thickness of layers, and band gaps. *Sol. Energy* **216**, 259–265 (2021).
64. Sadanand-Singh, P. K., Rai, S., Lohia, P. & Dwivedi, D. K. Comparative study of the CZTS, $CuSbS_2$ and $CuSbSe_2$ solar photovoltaic cell with an earth-abundant non-toxic buffer layer. *Sol. Energy* **222**, 175–185 (2021).
65. Garmim, T. *et al.* Effect of alternative buffer layers for SnS based solar cells: Numerical analysis using SCAPS-1D. *Mater. Today Proc.* **66**, 146–150 (2022).
66. Maharana, B., Jha, R. & Chatterjee, S. Metal oxides as buffer layers for CZTS based solar cells: A numerical analysis by SCAPS-1D software. *Opt. Mater. Amst.* **131**, 112734 (2022).
67. Riyad, M. N. H., Sunny, A., Khatun-Most, M., Rahman, S. & Ahmed, S. R. A. Performance evaluation of WS_2 as buffer and Sb_2S_3 as hole transport layer in CZTS solar cell by numerical simulation. *Eng. R Rep.* **5**, e12600 (2023).
68. Khattak, Y. H. *et al.* Effect of CZTSe BSF and minority carrier life time on the efficiency enhancement of CZTS kesterite solar cell. *Curr. Appl. Phys.* **18**, 633–641 (2018).
69. Hong, C. W. *et al.* Chemically deposited cds buffer/kesterite Cu_2ZnSnS_4 solar cells: Relationship between CdS thickness and device performance. *ACS Appl. Mater. Interfaces* **9**, 36733–36744 (2017).
70. Cantas, A. *et al.* Importance of CdS buffer layer thickness on Cu_2ZnSnS_4-based solar cell efficiency. *J. Phys. D Appl. Phys.* **51**, 275501 (2018).
71. Sun, Q. *et al.* Efficient environmentally friendly flexible CZTSSe/ZnO solar cells by optimizing ZnO buffer layers. *Materials* **16**, 2869 (2023).
72. Saadat, M., Amiri, O. & Mahmood, P. H. Potential efficiency improvement of $CuSb(S_{1-x}, Se_x)2$ thin film solar cells by the Zn(O, S) buffer layer optimization. *Sol. Energy* **225**, 875–881 (2021).
73. Welch, A. W. *et al.* Trade-offs in thin film solar cells with layered chalcostibite photovoltaic absorbers. *Adv. Energy Mater.* **7**, 1601935 (2017).
74. Rana, Md. S., Islam, Md. M. & Julkarnain, M. Enhancement in efficiency of CZTS solar cell by using CZTSe BSF layer. *Sol. Energy* **226**, 272–287 (2021).
75. Zhang, X., Yuan, Z. & Chen, S. Low electron carrier concentration near the p-n junction interface: A fundamental factor limiting short-circuit current of Cu(In, Ga)Se2 solar cells. *Sol. RRL* **3**, 1900057 (2019).
76. Walsh, A., Da Silva, J. L. F. & Wei, S.-H. Origins of band-gap renormalization in degenerately doped semiconductors. *Phys. Rev. B* **78**, 075211 (2008).
77. Xie, Y. *et al.* Enhancing photovoltaic performance of inverted planar perovskite solar cells by cobalt-doped nickel oxide hole transport layer. *ACS Appl. Mater. Interfaces* **10**, 14153–14159 (2018).
78. Kirchartz, T. *et al.* Sensitivity of the Mott-Schottky analysis in organic solar cells. *J. Phys. Chem. C* **116**, 7672–7680 (2012).
79. Basak, A. & Singh, U. P. Numerical modelling and analysis of earth abundant Sb_2S_3 and Sb_2Se_3 based solar cells using SCAPS-1D. *Sol. Energy Mater Sol. Cells* **230**, 111184 (2021).
80. Islam, M. T. & Thakur, A. K. Two stage modelling of solar photovoltaic cells based on Sb_2S_3 absorber with three distinct buffer combinations. *Sol. Energy* **202**, 304–315 (2020).
81. Shasti, M. & Mortezaali, A. Numerical study of Cu2O, SrCu2O2, and CuAlO2 as hole-transport materials for application in perovskite solar cells. *Phys. Status Solidi A* **216**, 1900337 (2019).
82. Pindolia, G., Shinde, S. M. & Jha, P. K. Optimization of an inorganic lead free RbGeI3 based perovskite solar cell by SCAPS-1D simulation. *Sol. Energy* **236**, 802–821 (2022).
83. Walkons, C., Murshed, R. & Bansal, S. Numerical analysis of Pb-free perovskite absorber materials: Prospects and challenges. *Sol. RRL* **4**, 2000299 (2020).
84. Roy, P. & Khare, A. Understanding the strategies to attain the best performance of all inorganic lead-free perovskite solar cells: Theoretical insights. *Int. J. Energy Res.* **46**, 15881–15899 (2022).
85. Wei, S.-H. & Zunger, A. Band offsets at the CdS/CuInSe2 heterojunction. *Appl. Phys. Lett.* **63**, 2549–2551 (1993).
86. Klenk, R. Characterisation and modelling of chalcopyrite solar cells. *Thin Solid Films* **387**, 135–140 (2001).
87. Minemoto, T. *et al.* Theoretical analysis of the effect of conduction band offset of window/CIS layers on performance of CIS solar cells using device simulation. *Sol. Energy Mater Sol. Cells* **67**, 83–88 (2001).
88. Minemoto, T. & Julayhi, J. Buffer-less Cu(In, Ga)Se2 solar cells by band offset control using novel transparent electrode. *Curr. Appl. Phys.* **13**, 103–106 (2013).
89. Minemoto, T. & Murata, M. Theoretical analysis on effect of band offsets in perovskite solar cells. *Sol. Energy Mater. Sol. Cells* **133**, 8–14 (2015).
90. Haider, M., Zhen, C., Wu, T., Liu, G. & Cheng, H.-M. Boosting efficiency and stability of perovskite solar cells with nickel phthalocyanine as a low-cost hole transporting layer material. *J. Mater. Sci. Technol.* **34**, 1474–1480 (2018).
91. Saikia, D., Bera, J., Betal, A. & Sahu, S. Performance evaluation of an all inorganic CsGeI3 based perovskite solar cell by numerical simulation. *Opt. Mater. Amst.* **123**, 111839 (2022).

92. Du, H.-J., Wang, W.-C. & Zhu, J.-Z. Device simulation of lead-free CH₃NH₃SnI₃ perovskite solar cells with high efficiency. *Chin. Phys. B* **25**, 108802 (2016).
93. Abdelaziz, S., Zekry, A., Shaker, A. & Abouelatta, M. Investigating the performance of formamidinium tin-based perovskite solar cell by SCAPS device simulation. *Opt. Mater. Amst.* **101**, 109738 (2020).
94. Guo, Q. *et al.* Fabrication of 7.2% efficient CZTSSe solar cells using CZTS nanocrystals. *J. Am. Chem. Soc.* **132**, 17384–17386 (2010).
95. Zhang, Z. *et al.* Over 10% efficient pure CZTSe solar cell fabricated by electrodeposition with Ge doping. *Sol. RRL* **4**, 2000059 (2020).
96. Taskesen, T. *et al.* Device characteristics of an 11.4% CZTSe solar cell fabricated from sputtered precursors. *Adv. Energy Mater.* **8**, 1703295 (2018).
97. Ren, Y. *et al.* Influence of the Cu₂ZnSnS₄ absorber thickness on thin film solar cells. *Phys. Status Solidi (a)* **212**, 2889–2896 (2015).
98. Deepthi, J. K. Bandgap tuning and input parameter optimization for lead-free all-inorganic single, double, and ternary perovskite-based solar cells. *Sol. RRL* **6**, 4 (2022).
99. Mora-Herrera, D., Silva-González, R., Cancino-Gordillo, F. E. & Pal, M. Development of Cu₂ZnSnS₄ films from a non-toxic molecular precursor ink and theoretical investigation of device performance using experimental outcomes. *Sol. Energy* **199**, 246–255 (2020).
100. Kanevce, A. & Gessert, T. A. Optimizing CdTe solar cell performance: Impact of variations in minority-carrier lifetime and carrier density profile. *IEEE J. Photovolt.* **1**, 99–103 (2011).
101. Duan, H.-S. *et al.* The role of sulfur in solution-processed Cu₂ZnSn(S, Se)4 and its effect on defect properties. *Adv. Funct. Mater.* **23**, 1466–1471 (2013).
102. Haider, S. Z., Anwar, H. & Wang, M. Theoretical device engineering for high-performance perovskite solar cells using CuSCN as hole transport material boost the efficiency above 25%. *Phys. Status Solidi A* **216**, 1900102 (2019).
103. Islam, T. *et al.* Simulation studies to quantify the impacts of point defects: An investigation of Cs₂AgBiBr6 perovskite solar devices utilizing ZnO and Cu₂O as the charge transport layers. *Comput. Mater. Sci.* **184**, 109865 (2020).
104. Yousefi, M., Minbashi, M., Monfared, Z., Memarian, N. & Hajjiah, A. Improving the efficiency of CZTSSe solar cells by engineering the lattice defects in the absorber layer. *Sol. Energy* **208**, 884–893 (2020).
105. Shin, B., Zhu, Y., Bojarczuk, N. A., Jay Chey, S. & Guha, S. Control of an interfacial MoSe2 layer in Cu2ZnSnSe4 thin film solar cells: 8.9% power conversion efficiency with a TiN diffusion barrier. *Appl. Phys. Lett.* **101**, 053903 (2012).
106. Krbal, M. *et al.* 2D MoSe₂ structures prepared by atomic layer deposition. *Phys. Status Solidi RRL Rapid Res. Lett.* **12**, 1800023 (2018).
107. Kaur, K., Kumar, N. & Kumar, M. Strategic review of interface carrier recombination in earth abundant Cu–Zn–Sn–S–Se solar cells: Current challenges and future prospects. *J. Mater. Chem. A Mater.* **5**, 3069–3090 (2017).
108. Song, Y. *et al.* Self-organized back surface field to improve the performance of Cu₂ ZnSn(S, Se)4 solar cells by applying P-Type MoS_e2: Nb to the back electrode interface. *ACS Appl. Mater. Interfaces* **11**, 31851–31859 (2019).
109. Li, J. *et al.* A Temporary barrier effect of the alloy layer during selenization: Tailoring the thickness of MoSe ₂ for efficient Cu₂ZnSnSe₄ solar cells. *Adv. Energy Mater.* **5**, 4 (2015).
110. Brammertz, G. *et al.* Characterization of defects in 9.7% efficient Cu2ZnSnSe4-CdS-ZnO solar cells. *Appl. Phys. Lett.* **103**, 16 (2013).
111. Sunny, A. & Ahmed, S. R. A. Numerical simulation and performance evaluation of highly efficient Sb₂Se₃ solar cell with tin sulfide as hole transport layer. *Phys. Status Solidi B* **258**, 2000630 (2021).
112. Ahmed, A., Riaz, K., Mehmood, H., Tauqeer, T. & Ahmad, Z. Performance optimization of CH₃NH₃Pb(I₁₋ₓBrₓ)₃ based perovskite solar cells by comparing different ETL materials through conduction band offset engineering. *Opt. Mater. Amst.* **105**, 109897 (2020).
113. Cao, Y. *et al.* Towards high efficiency inverted Sb₂Se₃ thin film solar cells. *Sol. Energy Mater Sol. Cells* **200**, 109945 (2019).
114. Hosen, A., Mian, M. S. & Ahmed, S. R. A. Improving the performance of lead-free FASnI3 -based perovskite solar cell with Nb2O5 as an electron transport layer. *Adv. Theory Simul.* **6**, 2 (2023).
115. Erkan, M. E., Chawla, V. & Scarpulla, M. A. Reduced defect density at the CZTSSe/CdS interface by atomic layer deposition of Al2O3. *J. Appl. Phys.* **119**, 19 (2016).
116. Kauk-Kuusik, M. *et al.* Detailed Insight into the CZTS/CdS interface modification by air annealing in monograin layer solar cells. *ACS Appl. Energy Mater.* **4**, 12374–12382 (2021).
117. Jeganath, K., George, S. D., Murari, M. S. & Raviprakash, Y. Probing the depth inhomogeneity of spray pyrolyzed CZTS thin films via chemical etching. *Inorg. Chem. Commun.* **145**, 109952 (2022).
118. Rijal, S. *et al.* Templated growth and passivation of vertically oriented antimony selenide thin films for high-efficiency solar cells in substrate configuration. *Adv. Funct. Mater.* **32**, 2110032 (2022).
119. Hwang, S. K. *et al.* Improved interfacial properties of electrodeposited Cu2ZnSn(S, Se)4 thin-film solar cells by a facile post-heat treatment process. *Prog. Photovolt. Res. Appl* **28**, 1345–1354 (2020).
120. Singh, P. & Ravindra, N. M. Analysis of series and shunt resistance in silicon solar cells using single and double exponential models. *Emerg. Mater. Res.* **1**, 33–38 (2012).
121. Jayan, K. D. High-efficiency non-toxic 2-terminal and 4-terminal perovskite-transition metal dichalcogenide tandem solar cells. *Adv. Theory Simul.* **5**, 5 (2022).
122. Raj, A., Kumar, M., Kumar, A., Laref, A. & Anshul, A. Investigating the potential of lead-free double perovskite Cs₂AgBiBr6 material for solar cell applications: A theoretical study. *Int. J. Energy Res.* **46**, 13801–13819 (2022).
123. Chakraborty, K., Choudhury, M. G. & Paul, S. Numerical study of Cs₂TiX₆ (X = Br−, I−, F− and Cl−) based perovskite solar cell using SCAPS-1D device simulation. *Sol. Energy* **194**, 886–892 (2019).

Acknowledgements

Author contributions

K.T.A.D.: methodology, validation, formal analysis, investigation, writing-original draft, M.K.H.: validation, formal analysis, investigation, L.M.: conceptualization, methodology, validation, formal analysis, investigation, writing-review& editing, visualization, project administration and supervision.

Competing interests

The authors declare no competing interests.

Additional information

Supplementary Information The online version contains supplementary material available at https://doi.org/10.1038/s41598-024-51711-6.

Correspondence and requests for materials should be addressed to L.M.

Reprints and permissions information is available at www.nature.com/reprints.

Publisher's note Springer Nature remains neutral with regard to jurisdictional claims in published maps and institutional affiliations.